



# Outstanding low-temperature performance for NH<sub>3</sub>-SCR of NO over broad Cu-ZSM-5 sheet with highly exposed *a*-c orientation

Xiaonan Guo<sup>a</sup>, Runduo Zhang<sup>a,\*</sup>, Zhaoying Di<sup>a</sup>, Bin Kang<sup>a</sup>, Hanxiao Shen<sup>a</sup>, Ying Wei<sup>a</sup>, Jingbo Jia<sup>a</sup>, Lirong Zheng<sup>b</sup>

<sup>a</sup> State Key Laboratory of Chemical Resource Engineering, Beijing Key Laboratory of Energy Environmental Catalysis, Beijing University of Chemical Technology, Beijing 100029, PR China

<sup>b</sup> Beijing Synchrotron Radiation Facility (BSRF), Institute of High Energy Physics, Chinese Academy of Sciences, Beijing 100049, PR China

## ARTICLE INFO

### Keywords:

Morphology control  
NH<sub>3</sub>-SCR  
Nanosheet ZSM-5 zeolite  
Copper species  
XAS

## ABSTRACT

Five ZSM-5-based catalysts with diverse zeolitic morphologies were prepared to experimentally investigate and computationally analyze the correlation between crystal plane and copper species. The types and numbers of copper species dispersed over Cu-ZSM-5 catalysts were emphatically determined to elucidate the structure-performance relationship of the Cu-ZSM-5 catalyst with broad sheet in the selective catalytic reduction (SCR) of NO by NH<sub>3</sub>. This study indicates that the broad Cu-ZSM-5 sheet exhibits outstanding low-temperature performance, achieving complete NO<sub>x</sub> removal at 250–550 °C. Operando X-ray absorption spectroscopy (XAS) experiments demonstrated this nanosheet catalyst has highly dispersed Cu<sup>2+</sup> ions as key active sites, which are facilely solubilized by NH<sub>3</sub> at low temperatures, further promoting rapid dynamic switching between Cu<sup>2+</sup> and Cu<sup>+</sup> species. And the density functional theory (DFT) calculations showed the Cu<sup>2+</sup> forms a unique interaction with the [010] crystal plane, leading to a lower energy barrier of the rate-determining step, resulting in extraordinary NO<sub>x</sub> conversion.

## 1. Introduction

In recent years, the global atmospheric environment has been gradually improved with significant abatement in heavy haze weather caused by nitrogen oxides (NO<sub>x</sub>) emissions. However, the challenge of secondary pollution such as acid rain, photochemical smog, and ozone, induced by NO<sub>x</sub> remains severe [1–3]. This accordingly resulted in a negative impact on ecosystems (e.g., soil acidification, biodiversity losses) as well as human health (e.g., respiratory and cardiovascular diseases, acute bronchitis) [4,5]. A key to control the secondary pollution is therefore focused on reducing the original NO<sub>x</sub> emission. Selective catalytic reduction of NO<sub>x</sub> by ammonia (NH<sub>3</sub>-SCR) has been widely used as the primary treatment technique for controlling NO<sub>x</sub> in exhaust gases from stationary sources such as cement kilns, industrial furnaces, and solid waste incineration plants [6–8]. For these industrial hazards, NH<sub>3</sub>-SCR systems are placed behind dust collectors and desulfurization units to solve problems such as catalyst abrasion and poisoning at low temperatures [9]. Conventional V<sub>2</sub>O<sub>5</sub>-WO<sub>3</sub>/TiO<sub>2</sub> catalysts were developed for industrial application at 300–400 °C, but their low-temperature

activities are difficult to be guaranteed, in addition to the narrow temperature window for NO<sub>x</sub> effective removal and the biological toxicity of VO<sub>x</sub> solids being fatal drawbacks [10,11]. Although Mn-based-oxide catalysts can show remarkable activities at low temperatures due to their good redox abilities, the production of large amounts of N<sub>2</sub>O reduces the corresponding N<sub>2</sub> selectivity [8,12,13]. Therefore, the development of catalysts with high deNO<sub>x</sub> activity and N<sub>2</sub> selectivity at low-temperature region is one of the hot spots in NH<sub>3</sub>-SCR research. Zeolite catalysts are of great interest for high specific surface area, variable acidity, and good thermal stability, as well as copper-based zeolite catalysts have shown excellent low-temperature SCR behaviors associated with high ammonia storage capacity to supply enough reducing agent [6,8]. ZSM-5 is a zeolite with MFI topology [two-dimensional 10-membered rings (MR) cross-pore structure], which has been extensively studied in the NH<sub>3</sub>-SCR reaction. However, it is a little difficult for the classical coffin-shaped Cu-ZSM-5 to avoid the formation of large amounts of CuO<sub>x</sub> clusters during calcination. Moreover, there is increasing evidence for the benefits of synthesizing nanosized zeolites with markedly reduced internal diffusion limitations

\* Corresponding author.

E-mail address: [zhangrd@mail.buct.edu.cn](mailto:zhangrd@mail.buct.edu.cn) (R. Zhang).

<https://doi.org/10.1016/j.apcatb.2023.123519>

Received 8 August 2023; Received in revised form 8 October 2023; Accepted 13 November 2023

Available online 17 November 2023

0926-3373/© 2023 Elsevier B.V. All rights reserved.

for enhanced performances in catalysis, adsorption, and even thermal stability [14–16]. According to the literature [17,18], the consideration on the dynamic diameters of chemical molecules involved into certain reactions with respect to the pore dimensions of diverse topological zeolites is necessary. As for  $\text{NH}_3$ -SCR reaction, the kinetic diameters of NO (0.32 nm),  $\text{NH}_3$  (~0.37 nm),  $\text{O}_2$  (0.35 nm),  $\text{N}_2$  (0.36 nm), and  $\text{H}_2\text{O}$  (~0.30 nm) are essentially smaller than the dimension of the dominated 10-MR pore of ZSM-5 zeolite (0.53 nm  $\times$  0.56 nm). In this case, the diffusion limitation is marginal. Nevertheless, the copper species in the hydrated state (such as  $[\text{Cu}(\text{H}_2\text{O})_6]^{2+}$  and  $[\text{Cu}(\text{OH})(\text{H}_2\text{O})_5]^+$ ) as well as those solvated by  $\text{NH}_3$  (such as  $[\text{Cu}(\text{II})(\text{NH}_3)_4]^{2+}$  and  $[\text{Cu}(\text{I})(\text{NH}_3)_2]^+$ ) with kinetic diameters larger than 0.56 nm might cause some diffusion restriction during the ion-exchange process [6]. The broad Cu-ZSM-5 sheet with highly exposed *a-c* orientation could be beneficial for enhancing the diffusion behaviors of copper complex precursors and promoting dispersion of active species to achieve a superior SCR performance. Since zeolites became well-known, the researchers were committed to the development of their morphologies by designing special organic structure-directing agents or fluoride shielding effects [19–21]. Ma et al. successfully synthesized self-pillared pentasil zeolite nanosheets with the thickness of 10–20 nm along the *b*-axis by designing pyridine-based cation as a template with the guidance of theoretical simulations, which were applied in methanol-to-propylene (MTP) reaction [19]. Dai et al. chose ammonium fluoride as a synthetic modifier for zeolites to obtain ultrathin zeolite plates by modifying the ratio of the crystal face aspects, and the platelike ZSM-5 zeolites exhibited a substantially extended lifetime in the methanol-to-hydrocarbons (MTH) reaction [20]. ZSM-5 zeolites with short straight channel characteristics are common in applications such as *n*-hexane aromatization, *n*-heptane cracking, depolymerization of waste plastics, and hydrogen generation from ammonia borane hydrolysis, where the advantages of two-dimensional nanosheet zeolites focus on the improved diffusion behaviors, better metal distribution, and less coke deposition [16, 21–23]. Zhang et al. point out that the thinner nanosheets exhibit superior performances (conversion, lifetime, and resistance to deactivation) in the catalytic cracking of *n*-heptane, which can be attributed to their larger surface areas and shorter straight channels beneficial for a fast diffusion [21]. Furthermore, Wang and co-workers demonstrated that zeolite nanosheets are ideal supports for anchoring various ultrasmall metallic species (e.g., Rh and Ru), facilitating the homogeneous dispersion of loaded sub-nanometallic clusters within the sinusoidal 5-MR of MFI framework and maintaining stability at high temperatures [16]. Although the above literature works have reported the potential use of broad nanosheet zeolite catalysts in various industrially important reactions, the application of nanosheet materials in SCR reaction and their properties such as redox ability and acidity correlating to catalytic behaviors have never been clearly demonstrated.

According to the previous works motioned above, we synthesized five Cu-ZSM-5 zeolite catalysts with different morphologies based on diverse facets, including large nanosheet ( $\text{NS}_\text{L}$ ), small nanosheet ( $\text{NS}_\text{S}$ ), nanorod (NR), nanoparticle (NP), and the conventional (Con) morphologies, and evaluated for the  $\text{NH}_3$ -SCR performances. First, morphologies, pore structure, and acidity of Cu-ZSM-5 zeolites were revealed by X-ray diffraction (XRD), scanning electron microscopy (SEM), transmission electron microscopy (TEM), high-resolution transmission electron microscopy (HR-TEM),  $\text{N}_2$  physisorption, temperature-programmed desorption of  $\text{NH}_3$  ( $\text{NH}_3$ -TPD), solid-state  $^{27}\text{Al}$  and  $^{29}\text{Si}$  magic angle spinning (MAS) nuclear magnetic resonance (NMR) spectra. Then, this paper focuses on the detailed status of copper species, which were preliminarily revealed by characterization techniques of temperature-programmed reduction by hydrogen ( $\text{H}_2$ -TPR), X-ray photoelectron spectroscopy (XPS), electron paramagnetic resonance (EPR), and inductively coupled plasma-atomic emission spectrometry (ICP-AES). Most important of all, the fine structure of copper species and their microscopic variation were illuminated by operando X-ray absorption near edge structure (XANES) and extended X-ray absorption

fine structure (EXAFS) spectroscopies, while the DFT calculations were successively used to discuss the trend of the energy barriers of different copper species on distinct crystal planes to further reveal the structure-performance relationship of the nanosheet Cu-ZSM-5 zeolite, aiming to design zeolite with more beneficial copper ions through a strategy to selectively exposure the specific crystal surface to obtain an excellent low-temperature  $\text{NH}_3$ -SCR performance.

## 2. Experimental

### 2.1. Catalyst preparation

Except for the conventional ZSM-5 zeolite (Con-ZSM-5) and nanoparticle one (NP-ZSM-5) synthesized by one-pot hydrothermal method, other ZSM-5 zeolites [nanosheet-large ( $\text{NS}_\text{L}$ -ZSM-5), nanosheet-small ( $\text{NS}_\text{S}$ -ZSM-5), nanorod (NR-ZSM-5)] with different morphologies were synthesized by seed-assisted method. The preparation method of Con-ZSM-5,  $\text{NS}_\text{S}$ -ZSM-5, NP-ZSM-5, and NR-ZSM-5 as well as the process for obtaining copper ion-exchanged zeolites are described in [Supporting Information \(SI\)](#). The chemical reagents involved in the preparation of zeolites also refer to SI.

$\text{NS}_\text{L}$ -ZSM-5 zeolite was synthesized by combining preliminary aging with a fluoride-assisted low-temperature crystallization [20]. On the one hand, the addition of ammonium fluoride ( $\text{NH}_4\text{F}$ ) destroyed the gel structure and generated critical nanoparticles to form the platelike crystals. On the other hand, decreasing the pH values and thus changing the solubility of silica species. Furthermore, the fluoride tends to adsorb on the [010] crystal plane and covalently bonds with framework Si atoms to form the  $[\text{SiO}_2\text{F}]^-$  units, further controlling the orientation of the  $\text{TPA}^+$  template along the *a-c* plane to obtain *b*-axis oriented nanosheets [20]. The broad MFI zeolite synthesis was conducted with the molar compositions of 1.0  $\text{SiO}_2$  : 0.025  $\text{Al}_2\text{O}_3$  : 0.1  $\text{TPAOH}$  : 0.8  $\text{NH}_4\text{F}$  : 30  $\text{H}_2\text{O}$ . 16.59 mL tetraethyl orthosilicate (TEOS) was added together with 0.28 g pseudo boehmite, 6.03 g tetrapropylammonium hydroxide solution (TPAOH, 25 wt%), and 17.5 mL  $\text{H}_2\text{O}$  at room temperature simultaneously with stirring at 90 °C for 12 h. The above step completes the initial crystallization of broad zeolite. Then, 2.22 g  $\text{NH}_4\text{F}$  and 18 mL  $\text{H}_2\text{O}$  were added to the crystallized liquids and continued stirring at constant temperature for 12 h. Finally, the obtained mixture was transferred into a 100 mL Teflon-lined stainless-steel autoclave and crystallized at 170 °C for 3 days under autogenous pressure.

Con-ZSM-5,  $\text{NS}_\text{S}$ -ZSM-5, NP-ZSM-5, and NR-ZSM-5 zeolites were synthesized following the literature [21,22,24,25].

### 2.2. Catalyst characterization

The physicochemical properties of Cu-ZSM-5 catalysts were examined by XRD, SEM, TEM, HR-TEM,  $\text{N}_2$  physisorption, ICP-AES,  $^{27}\text{Al}$  and  $^{29}\text{Si}$  MAS NMR,  $\text{NH}_3$ -TPD,  $\text{H}_2$ -TPR,  $\text{N}_2\text{O}$  chemisorption, XPS, EPR, and Cu K-edge XAFS spectroscopy. The specific characterization procedures are discussed in details in the SI.

### 2.3. Activity measurement

The concentration of exhaust gases ( $\text{N}_2\text{O}$ , NO,  $\text{NO}_2$ , and  $\text{NH}_3$ ) was monitored by Fourier Transform Infrared (FTIR) gas analyzer. Typically, 75 mg of the catalyst was loaded in a quartz fixed-bed reactor (0.6 cm i. d.) under an atmosphere composition of 1000 ppm NO, 1000 ppm  $\text{NH}_3$ , 8 vol%  $\text{O}_2$ , and 5%  $\text{H}_2\text{O}$ , balanced by He at a total flow rate of ~130 mL  $\text{min}^{-1}$  (GHSV = ~50,000  $\text{h}^{-1}$ ). Additionally, 10%  $\text{H}_2\text{O}$  and 200 ppm  $\text{SO}_2$  were added to the feed gas to evaluate the humidity resistance and  $\text{SO}_2$  tolerance of the catalysts.

### 2.4. Theoretical computation

Periodic density functional theory (DFT) calculations were

performed using the Vienna *ab-initio* simulation package (VASP) [26]. The MFI structure consists of 96 T atoms (T = Si, Al) and 192 oxygen atoms. Si atoms are substituted by one or two Al atoms in the 6-MR of corresponding crystal planes and the negative charges are generated. Subsequently, the copper species act as cations to compensate for the negative charge on the framework. The lattice parameters of MFI unit cell were set to  $a = 20.078 \text{ \AA}$ ,  $b = 19.894 \text{ \AA}$ , and  $c = 13.372 \text{ \AA}$  [27]. In the direction perpendicular to the different crystal planes, a large vacuum of  $15 \text{ \AA}$  is used to eliminate the effect among supercells.

The projector augmented wave (PAW) method combined with a plane wave basis set was used to describe the core and valence electrons [28]. The exchange correlation effects are investigated within the generalized gradient approximation according to Perdew, Burke, and Ernzerhof (PBE) [29]. The spin-polarized calculations were also taken into account and the cutoff energy was set to  $400 \text{ eV}$ . All structures were relaxed until the forces over each atom were smaller than  $0.05 \text{ eV \AA}^{-1}$  and electronic energies were converged within  $10^{-6} \text{ eV}$ . The gamma-centered k-points of  $1 \times 1 \times 1$  was selected for the Brillouin zone integration. The energy and location of transition states (TS) were calculated by the climbing-image nudged elastic band (CI-NEB) method, and the reasonable numbers of NEB images were chosen for transition states calculations [30].

### 3. Results and discussion

#### 3.1. Catalyst morphology and crystal structure

Fig. 1 shows the XRD patterns of Cu-ZSM-5 zeolites with different morphologies. All samples are confirmed to be MFI framework topology without any impurity phase, and the prepared samples were determined to have quite high crystallinity by the intensity of diffraction peaks at  $7.9^\circ$ ,  $8.8^\circ$ ,  $23.2^\circ$ ,  $23.9^\circ$ , and  $24.4^\circ$  [20–25]. Compared to other zeolites, the  $\text{NS}_\text{L}$ -Cu-ZSM-5 zeolite has the sharpest  $h0l$  reflections in XRD pattern, implying it has the best long-range order in  $a$ - $c$  orientation [31]. In addition, the  $\text{NS}_\text{L}$ -Cu-ZSM-5 and  $\text{NS}_\text{S}$ -Cu-ZSM-5 zeolites display lower peak intensity and greater full-width half-maxima (FWHM) at the  $010$  reflection (Table S1) with respect to Con-Cu-ZSM-5 and NR-Cu-ZSM-5, which further demonstrates the very limited growth of the nanosheet zeolites in the  $b$ -axis direction [32]. Besides, the wide and low intensity peaks are considered to be a typical characteristic of small particles in NP-Cu-ZSM-5, and it has the smallest apparent crystallinity [25,33]. The

crystallite size and relative crystallinity of the as-prepared Cu-ZSM-5 catalysts are presented in Table S1. For all Cu-ZSM-5 catalysts, no diffraction peaks belonging to  $\text{CuO}_x$  species were observed at  $35.6^\circ$  and  $38.8^\circ$ , which was possibly due to the highly dispersed of copper species, low  $\text{CuO}_x$  clusters content or small crystal size of  $\text{CuO}_x$  clusters.

As shown in Fig. 2, the SEM, TEM, and HR-TEM images were collected to display the morphologies of the zeolites and their prior crystal planes exposed [34]. As illustrated in Table 1, since the dimension evaluation by XRD is only reliable in the case of single crystal with a particle size large enough, the aspect ratio  $[(c+a)/b]$  was estimated from SEM images and followed an order as  $\text{NS}_\text{L}$ -Cu-ZSM-5 (115) >  $\text{NS}_\text{S}$ -Cu-ZSM-5 (12) > NR-Cu-ZSM-5 (8) > NP-Cu-ZSM-5 (2) = Con-Cu-ZSM-5 (2). The dimensional relationships for the Cu-ZSM-5 zeolites with different morphologies are illustrated in Scheme S1. Among them, the Con-Cu-ZSM-5 and NP-Cu-ZSM-5 are similar in aspect ratio, but the crystal size of NP-Cu-ZSM-5 is six times smaller than that of Con-Cu-ZSM-5 (Fig. 2A, J). The nanosheet samples with short distance for the straight channel are exposed between approximately 20–40 nm (Fig. 2D, G), in addition, both  $\text{NS}_\text{L}$ -Cu-ZSM-5 and  $\text{NS}_\text{S}$ -Cu-ZSM-5 observed by SEM are platelike and ultrathin [20,21]. As shown in Fig. 2J, M; NP-Cu-ZSM-5 is composed of particles with an average size of 50–100 nm, while NR-Cu-ZSM-5 exhibits an aggregated assembly of the stacked nanorods [22]. Specific surface areas in the HR-TEM image were selected for Fast Fourier Transformation (FFT) to further reveal their surface crystal planes. As shown in Fig. 2F, I; the bright spots of the collected FFT patterns are basically similar and could be indexed according to the diffraction patterns of the MFI along the  $[010]$  crystal plane [34]. Besides, the  $\text{NS}_\text{L}$ -Cu-ZSM-5 and  $\text{NS}_\text{S}$ -Cu-ZSM-5 single-layer nanosheets showed unique morphologies as well as electron beam transmission, and the lattice striations on the  $[010]$  crystal plane were clear and regular, indicating these catalysts being with a certain thinness [35]. Their HR-TEM and FFT images (Fig. 2E, F, H, I) exhibit a typical MFI straight channel along this  $[010]$  facet, which results in low-intensity peaks at greater FWHM in their XRD patterns [32].

$\text{N}_2$  adsorption-desorption isotherms and pore-size distributions of the Cu ion-exchange zeolites with distinct morphologies are depicted in Fig. 3a. All the adsorption isotherms rise rapidly in the relatively low-pressure region ( $P/P_0 < 0.02$ ), which proves that the as-prepared samples have microporous structures [35]. All samples, except Con-Cu-ZSM-5 zeolite which only have type I isotherm characteristics, were considered to be composite isotherms on the basis of type I isotherm, which also have type II isotherms for  $\text{NS}_\text{S}$ -Cu-ZSM-5 and NP-Cu-ZSM-5, and type IV isotherms for  $\text{NS}_\text{L}$ -Cu-ZSM-5 and NR-Cu-ZSM-5. With the increase of adsorption with  $P/P_0$ , an H4-type hysteresis loop appears between adsorption and desorption branches of  $\text{NS}_\text{L}$ -Cu-ZSM-5 and NR-Cu-ZSM-5 at relative pressures ( $0.45 < P/P_0 < 0.95$ ), which proved mesoporous structures existing in these samples. The mesoporous structure acts as a secondary pore system possibly providing highways for mobile  $[\text{Cu}(\text{II})(\text{H}_2\text{O})_6]^{2+}$ ,  $[\text{Cu}(\text{II})(\text{OH})(\text{H}_2\text{O})_5]^+$ ,  $\text{NH}_3$ -solvated  $[\text{Cu}(\text{II})(\text{NH}_3)_4]^{2+}$  and  $[\text{Cu}(\text{I})(\text{NH}_3)_2]^+$  complexes in diffusion [36]. For  $\text{NS}_\text{S}$ -Cu-ZSM-5 and NP-Cu-ZSM-5, the hysteresis loop observed at high relative pressure region ( $P/P_0 > 0.95$ ) is caused by the pseudo-mesoporous piling up between the small grains, and indicates that there are some mesoporous or macroporous structures existing in these nanoparticles, contributing to an obvious increase of BET surface area, especially the external surface area (Table 1) [37]. As illustrated in Table 1, the specific surface areas of copper-exchanged samples follow an order: NP-Cu-ZSM-5 ( $457 \text{ m}^2/\text{g}$ ) >  $\text{NS}_\text{L}$ -Cu-ZSM-5 ( $454 \text{ m}^2/\text{g}$ ) >  $\text{NS}_\text{S}$ -Cu-ZSM-5 ( $453 \text{ m}^2/\text{g}$ ) > Con-Cu-ZSM-5 ( $414 \text{ m}^2/\text{g}$ ) > NR-Cu-ZSM-5 ( $401 \text{ m}^2/\text{g}$ ). The  $\text{NS}_\text{L}$ -Cu-ZSM-5 and  $\text{NS}_\text{S}$ -Cu-ZSM-5 catalysts show superior BET surface areas, which provide sufficient evidence that the excellent BET surface area could promote the formation of ideal copper species and their well dispersion.

The coordination of Al atoms in the Cu-ZSM-5 zeolites with different morphologies was studied by  $^{27}\text{Al}$  MAS NMR (Fig. 4a). All samples show the main NMR peaks at  $\sim 53 \text{ ppm}$ , which belong to the tetra-coordinated

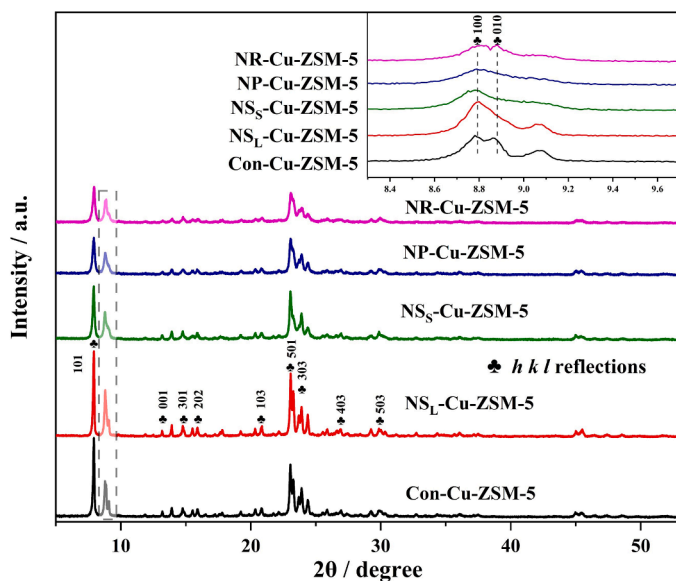
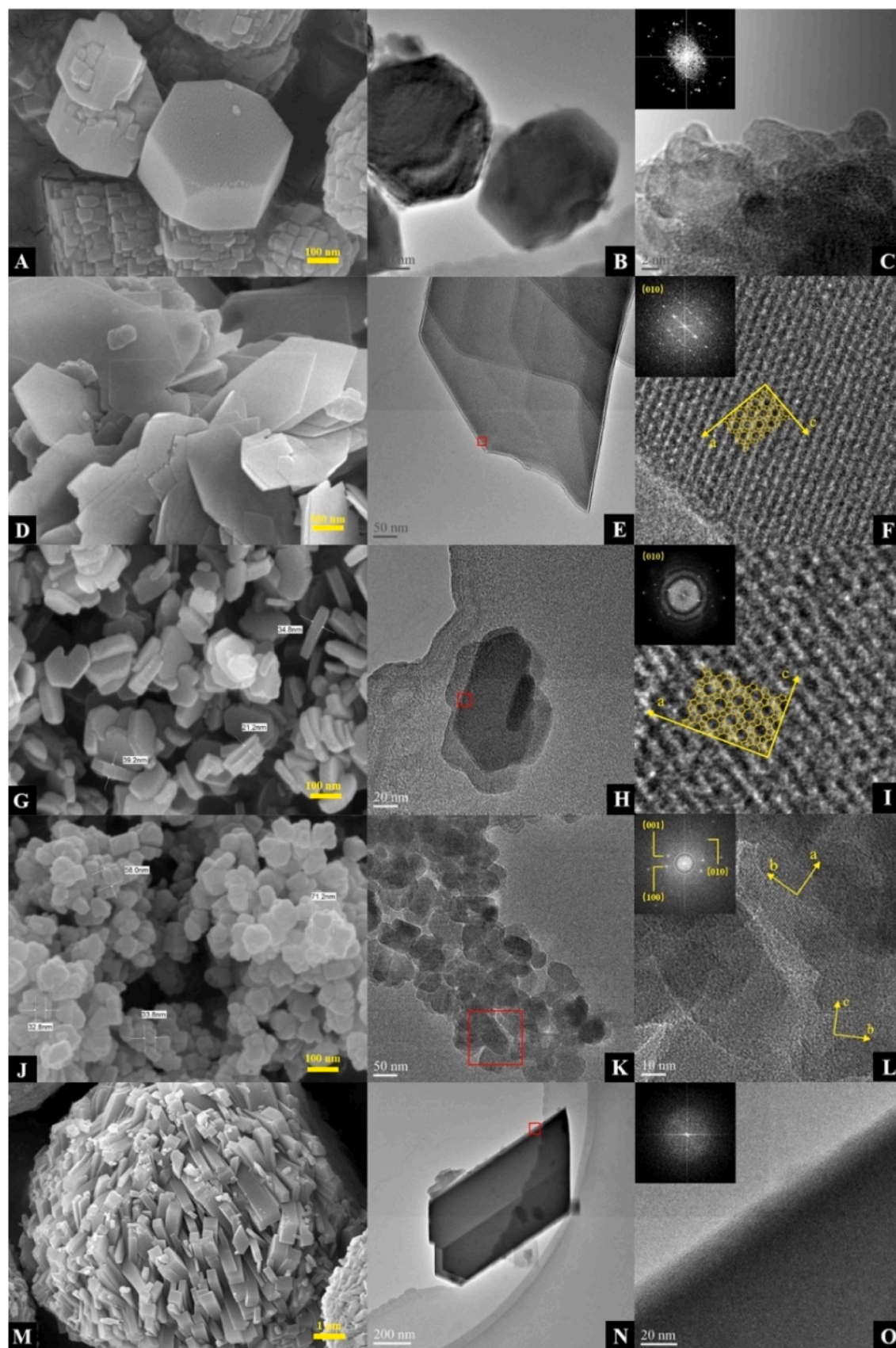


Fig. 1. XRD patterns of Cu ion-exchange ZSM-5 catalysts with diverse zeolitic morphologies.





**Fig. 2.** SEM, TEM, and HR-TEM images of the copper ion-exchanged zeolites Con-Cu-ZSM-5 (A, B, C), NS<sub>L</sub>-Cu-ZSM-5 (D, E, F), NS<sub>S</sub>-Cu-ZSM-5 (G, H, I), NP-Cu-ZSM-5 (J, K, L), NR-Cu-ZSM-5 (M, N, O). Fast Fourier transform (FFT) of (C), (F), (I), (L), and (O) are shown in their insets.



**Table 1**  
BET surface area, external surface area, aspect ratio, and dispersion.

Sample	$S_{\text{BET}}$ ( $\text{m}^2/\text{g}$ ) <sup>a</sup>	$S_{\text{ext}}$ ( $\text{m}^2/\text{g}$ ) <sup>b</sup>	Aspect ratio [(c+a)/b] <sup>c</sup>	Dispersion <sup>d</sup>	Crystal plane
Con-Cu-ZSM-5	414	58	2	0.57	-
NS <sub>L</sub> -Cu-ZSM-5	454	38	115	0.73	[010]
NS <sub>S</sub> -Cu-ZSM-5	453	74	12	0.66	[010]
NP-Cu-ZSM-5	457	94	2	0.63	-
NR-Cu-ZSM-5	401	78	8	0.53	-

<sup>a</sup>  $S_{\text{BET}}$  was calculated by Brunauer-Emmett-Teller (BET) method.

<sup>b</sup>  $S_{\text{micro}}$  was calculated by  $t$ -plot method. And  $S_{\text{ext}} = S_{\text{BET}} - S_{\text{micro}}$ .

<sup>c</sup> The aspect ratio [(c+a)/b] was roughly estimated from SEM images.

<sup>d</sup> Dispersion calculated based on the dissociative  $\text{N}_2\text{O}$  adsorption.

framework Al species [Al(IV)], however, a weak peak belonging to the hexa-coordinated extra-framework Al species [Al(VI)] at approximately 0 ppm can be observed, especially for the NP-Cu-ZSM-5 sample [38–40]. Large numbers of hexa-coordinated extra-framework Al species might lead to a low exchange rate of copper ions, instead of increasing the likelihood of  $\text{CuO}_x$  clusters.  $^{29}\text{Si}$  MAS NMR (Fig. 4b) was selected to explore the crystallinity of zeolites and the coordination state of Si and Al atoms in the zeolite skeleton, and the framework Si/Al ratios of Cu-ZSM-5 zeolites were calculated according to Loewenstein's rule and represented in Table 2 [41]. The spectra were dominated by the main peak at  $-113$  ppm and weak peak at  $-105$  ppm, which are assigned to the Si (4Si, 0Al) sites and Si (3Si, 1Al) sites, respectively [41,42]. Strong resonance at about  $-113$  ppm was observed in all zeolites with different morphologies, along with merely weak resonances at  $-105$  ppm, which confirmed the high crystallinity and relatively stable framework Si of these samples (Table S4) [14,41]. Analyses on the Si/Al ratios of ZSM-5 zeolites with different morphologies are detailed in Table 2 of the following section.

### 3.2. Characterization of copper species

In order to evaluate the concentration and strength of acid sites,  $\text{NH}_3$ -TPD measurements were carried out on Cu-ZSM-5 zeolites with diverse morphologies, and the results are shown in Fig. 5. Three main desorption peaks can be distinguished in the obtained desorption profiles. As believed by Gao and other researchers [42–46], the weak acid sites at about  $190^\circ\text{C}$  ( $\alpha$  sites) are assigned to the weakly adsorbed  $\text{NH}_3$  on the

weak Lewis acid of extra-framework Al sites and the structure of terminal hydroxyl, the medium acid sites at about  $240^\circ\text{C}$  ( $\beta$  sites) are thought to be induced by the substitution of surface protons by copper ions, representing the amount of ammonia adsorbed on the copper ions, and the strong acid sites at about  $360^\circ\text{C}$  ( $\gamma$  sites) are attributed to the  $\text{NH}_3$  adsorption on the structural Brønsted acid sites of Si-OH-Al bonds. The Pyridine-IR study (Fig.S9) provided solid evidence for the assignment of  $\text{NH}_3$ -TPD signals. The low-temperature  $\text{NH}_3$ -TPD peak associated with weak adsorption strength is assigned to Lewis acid sites, while the high-temperature one is assigned to Brønsted acid sites. The quantitative  $\text{NH}_3$  adsorption was calculated according to the TCD signals and the deconvolution by Gaussian method, as shown in Fig. 5b. The density of strong acid sites on Cu-ZSM-5 zeolites decreases in the order: NR-Cu-ZSM-5 > NS<sub>L</sub>-Cu-ZSM-5 > NS<sub>S</sub>-Cu-ZSM-5 > Con-Cu-ZSM-5 > NP-Cu-ZSM-5. This means that NR-Cu-ZSM-5, NS<sub>L</sub>-Cu-ZSM-5, and NS<sub>S</sub>-Cu-ZSM-5 are more beneficial to stabilize the adsorbed  $\text{NH}_3$ , which are not easy to be released and likely inhibit the formation of  $\text{N}_2\text{O}$  [47]. Combined with  $^{27}\text{Al}$  and  $^{29}\text{Si}$  MAS NMR experiments, we further explained the reasons for the difference in acidity. The total amount of acid sites decreases simultaneously with the increase of the framework Si/Al ratios. The total acid quantity of NR-Cu-ZSM-5 ( $1.30 \text{ mmol g}^{-1}$ ) is obviously larger than the other samples, because its framework Si/Al ratio (18.3) is the lowest [45]. Whereas, the NP-Cu-ZSM-5 catalyst had the highest framework Si/Al ratio, and its extra-framework Al inhibits more  $\text{NH}_3$  being stably adsorbed. In addition, it is apparent that the nanosheet samples expose relatively more medium acid sites, which also benefits for  $\text{NH}_3$  reserves, especially for the NS<sub>L</sub>-Cu-ZSM-5 sample [48].

The distribution of copper species had a profound effect on the redox capacity of SCR performance. As depicted in Fig. 6, the  $\text{H}_2$ -TPR curves of copper ion-exchanged zeolites consist of three visible reduction peaks distributed in  $250\text{--}350^\circ\text{C}$ ,  $350\text{--}500^\circ\text{C}$ , and  $500\text{--}750^\circ\text{C}$ , which are assigned to the reduction of isolated  $\text{Cu}^{2+}$  to  $\text{Cu}^+$ , the reduction of  $\text{CuO}_x$  clusters to  $\text{Cu}^0$ , and the reduction of isolated  $\text{Cu}^+$  ions to metallic  $\text{Cu}^0$ , respectively [49–52]. It is worth noting that the reduction of copper species on zeolites is generally divided into two categories, one is the direct reduction of  $\text{CuO}_x$  clusters to  $\text{Cu}^0$  (peak  $\beta$ ), and the other is the successive two-step reduction of copper ions to  $\text{Cu}^0$  [e.g.,  $\text{Cu}^{2+} \rightarrow \text{Cu}^+$  (peak  $\alpha$ ), and then  $\text{Cu}^+ \rightarrow \text{Cu}^0$  (peak  $\gamma$ )]. Therefore, the reduction peak  $\gamma$  assigned to  $\text{Cu}^+ \rightarrow \text{Cu}^0$  involves the  $\text{Cu}^+$  ions reduced from  $\text{Cu}^{2+}$  ions as well as the originally existing  $\text{Cu}^+$  ions over the zeolite. The lowest reduction temperature ( $314^\circ\text{C}$ ) observed in NS<sub>L</sub>-Cu-ZSM-5 demonstrates that the isolated  $\text{Cu}^{2+}$  ions in the NS<sub>L</sub>-Cu-ZSM-5 sample are the most easily reduced one, followed by NS<sub>S</sub>-Cu-ZSM-5 ( $321^\circ\text{C}$ ), Con-Cu-ZSM-5 ( $331^\circ\text{C}$ ), NP-Cu-ZSM-5 ( $335^\circ\text{C}$ ), and NR-Cu-ZSM-5

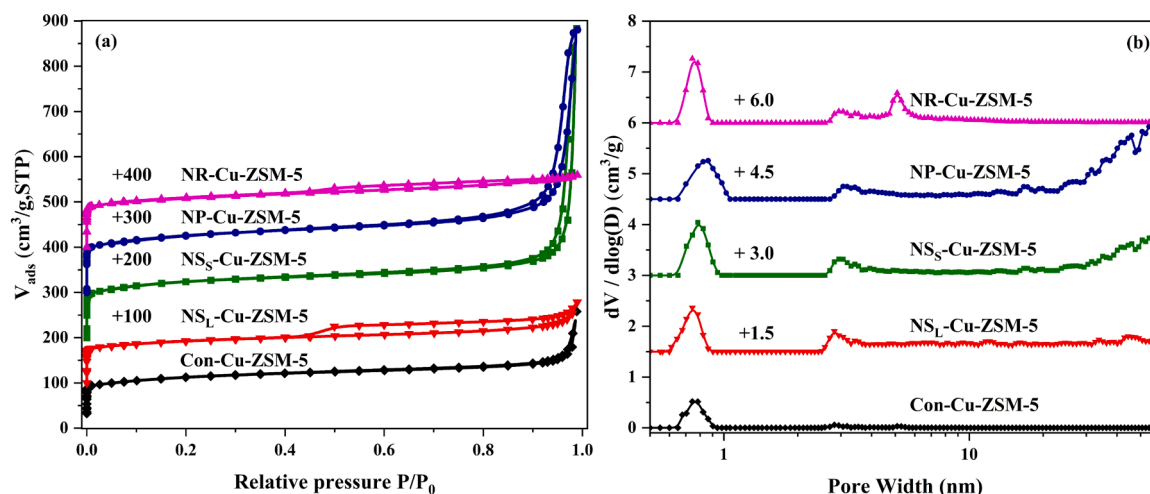


**Fig. 3.**  $\text{N}_2$  adsorption-desorption isotherms (a) and NLDFT pore-size distributions (b) of the Cu-ZSM-5 catalysts with diverse zeolitic morphologies.

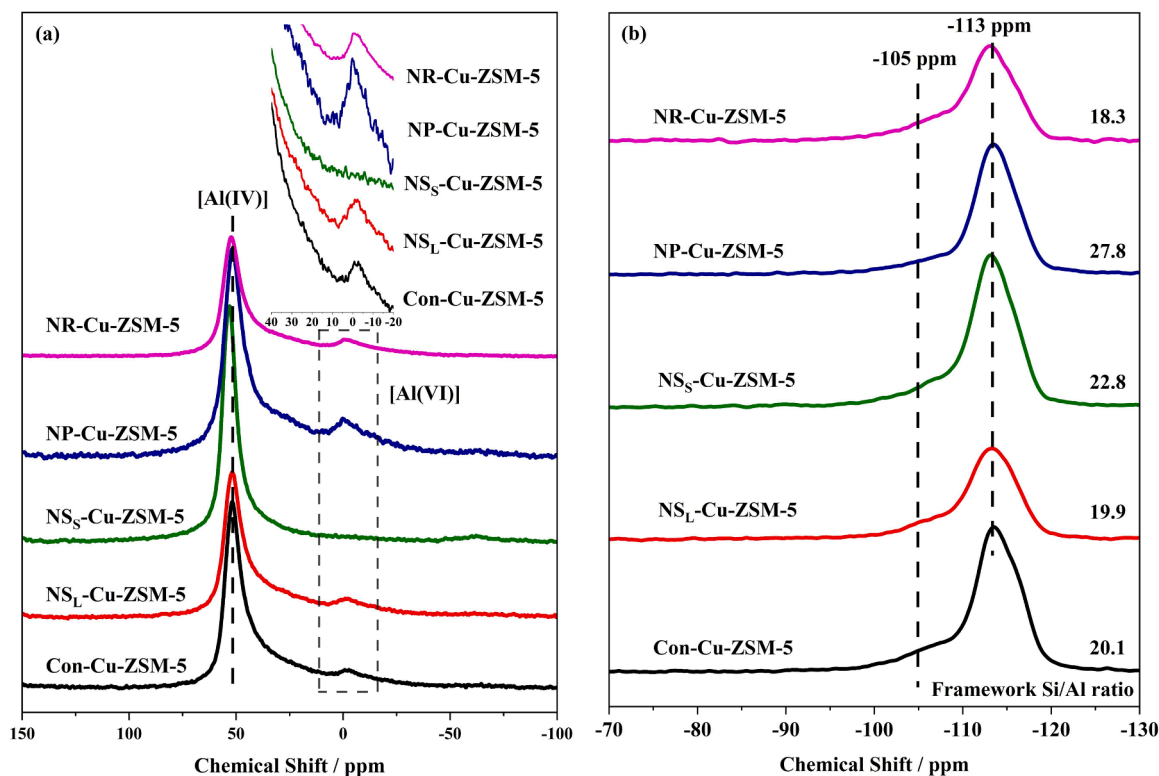


Fig. 4.  $^{27}\text{Al}$  MAS NMR (a) and  $^{29}\text{Si}$  MAS NMR (b) spectra of Cu-ZSM-5 catalysts with diverse zeolitic morphologies.

Table 2

Metal loading, Si/Al ratio of zeolite by ICP-AES, XPS, and  $^{29}\text{Si}$  MAS NMR.

Sample	Si/Al ratio by ICP <sup>a</sup>	Cu content (wt%) <sup>a</sup>	Si/Al ratio by XPS <sup>b</sup>	Cu content (wt%) <sup>b</sup>	Si/Al ratio by NMR <sup>c</sup>
Con-Cu-ZSM-5	19.4	0.805	13.3	0.66	20.1
$\text{NS}_\text{L}$ -Cu-ZSM-5	18.9	0.800	18.2	0.52	19.9
$\text{NS}_\text{s}$ -Cu-ZSM-5	22.9	0.883	20.2	0.52	22.8
NP-Cu-ZSM-5	19.2	0.733	16.2	0.41	27.8
NR-Cu-ZSM-5	17.7	0.898	17.9	0.98	18.3

<sup>a</sup> the Si/Al ratio and Cu content of the bulk were analyzed by ICP-AES.

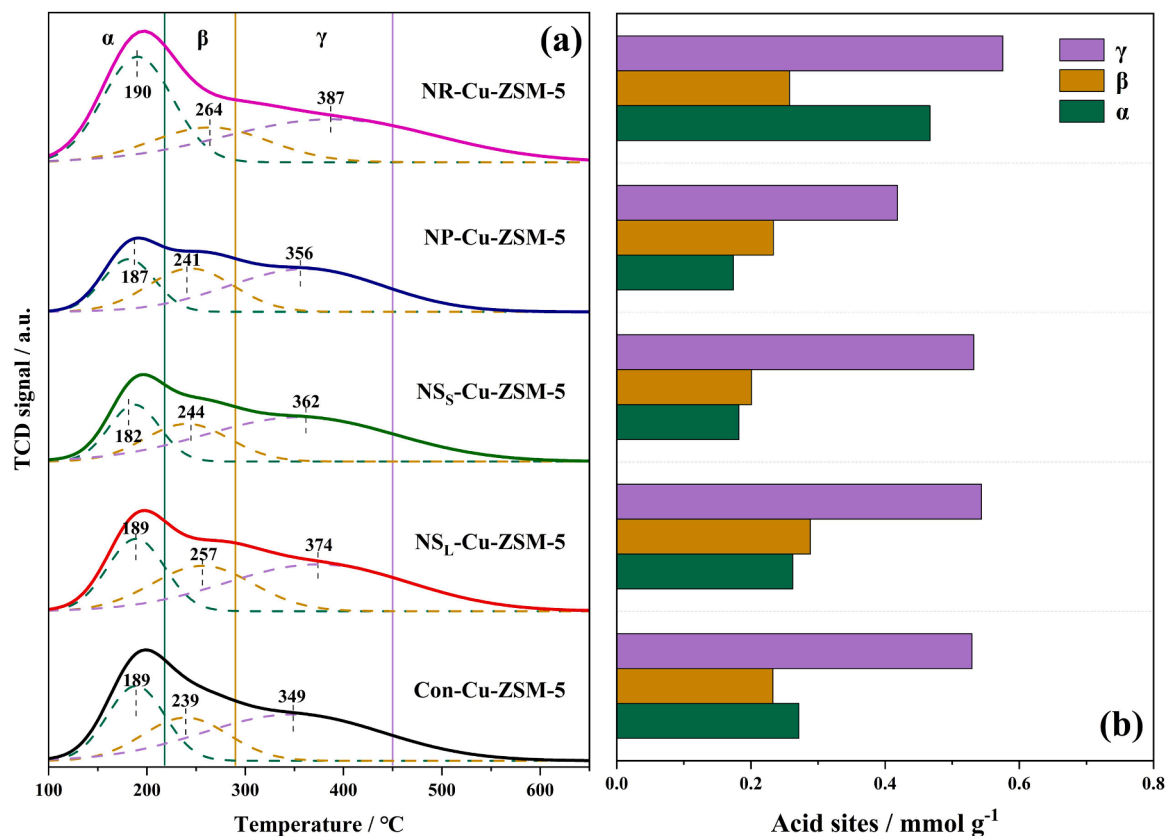
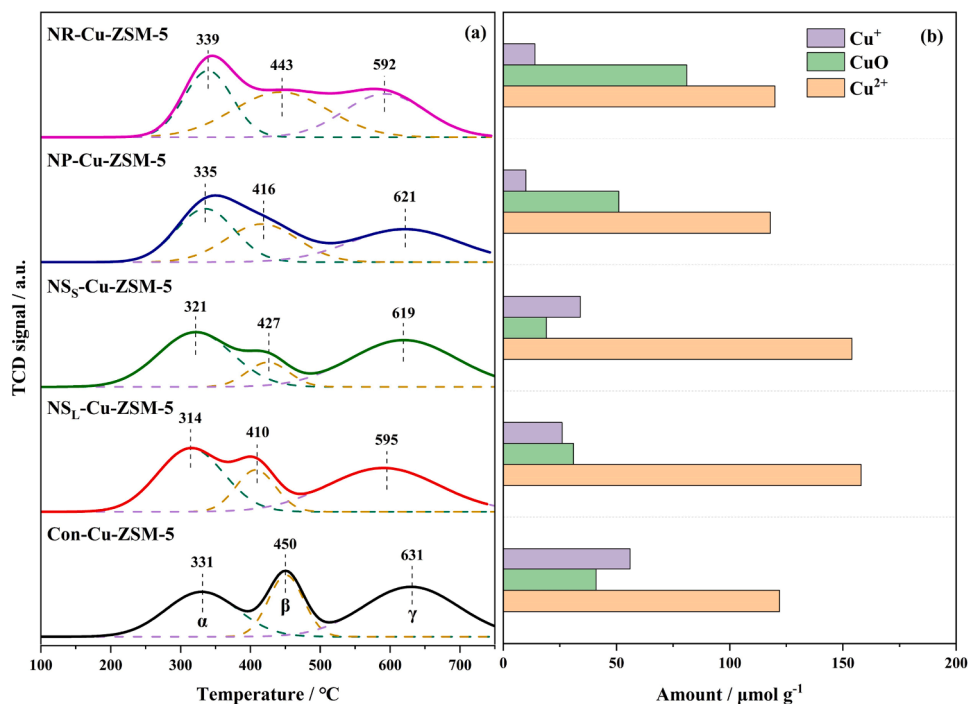
<sup>b</sup> the Si/Al ratio and Cu content of the surface were analyzed by XPS.

<sup>c</sup> the Si/Al ratio of the framework was analyzed by  $^{29}\text{Si}$  MAS NMR.

(339 °C). Besides, the  $\text{NS}_\text{L}$ -Cu-ZSM-5 and  $\text{NS}_\text{s}$ -Cu-ZSM-5 samples show fewer  $\text{CuO}_\text{x}$  species in comparison with the other samples and the amount of isolated Cu ions diminished in the following order:  $\text{NS}_\text{s}$ -Cu-ZSM-5 >  $\text{NS}_\text{L}$ -Cu-ZSM-5 > Con-Cu-ZSM-5 > NP-Cu-ZSM-5 > NR-Cu-ZSM-5 (Fig. 6 and Table S5). Particularly, large quantities of copper oxide clusters were detected in Con-Cu-ZSM-5, NP-Cu-ZSM-5, and NR-Cu-ZSM-5 catalysts, implying that the sheet samples promote the dispersion of copper ions. As illustrated in Table 1, the dispersion of copper species follows an order:  $\text{NS}_\text{L}$ -Cu-ZSM-5 (0.73) >  $\text{NS}_\text{s}$ -Cu-ZSM-5 (0.66) > NP-Cu-ZSM-5 (0.63) > Con-Cu-ZSM-5 (0.57) > NR-Cu-ZSM-5 (0.53), which was confirmed by  $\text{N}_2\text{O}$  chemisorption. The three-dimensional large grains or aggregated samples are limited in diffusion, making it difficult to exchange more dispersed copper ions at the Al sites. However,  $\text{H}_2$ -TPR, as a semi-quantification method, has limitations in distinguishing between  $\text{Cu}^{2+}$  and  $[\text{Cu}(\text{OH})]^+$  species. Next, the dehydrated and hydrated EPR spectra give measure of  $\text{Cu}^{2+}$  sites and total isolated  $\text{Cu}^{2+}$  ions,

respectively.

As shown in Fig. 7, XPS measurements for the Cu 2p region were conducted to further demonstrate the chemical state and surface composition of the copper species on Cu-ZSM-5. According to previous reports [53–55], the peaks at  $952.5 \pm 0.2$  and  $932.4 \pm 0.2$  eV are owned by the binding energy (BE) of Cu  $2\text{p}_{1/2}$  and Cu  $2\text{p}_{3/2}$  states of  $\text{Cu}^+$  species, respectively. Correspondingly, the BE peaks at  $953.7 \pm 0.2$  and  $934.2 \pm 0.2$  eV belong to the  $\text{Cu}^{2+}$  species in the Cu  $2\text{p}_{1/2}$  and Cu  $2\text{p}_{3/2}$  states, respectively. The dispersed  $\text{Cu}^{2+}$  ions corresponding to the peak at 940.5 eV are quantified by the unique satellite peak area, and the peak at 938.5 eV assigned to  $\text{Cu}^{2+}$  in CuO can also be detected (Table S6) [56]. Apparent satellite peak at 940.5 eV can be identified in  $\text{NS}_\text{L}$ -Cu-ZSM-5 and  $\text{NS}_\text{s}$ -Cu-ZSM-5 samples, implying that more dispersed  $\text{Cu}^{2+}$  ions appeared on their surfaces [17]. However, a large amount of CuO species is accumulated on the surface of the NP-Cu-ZSM-5 and NR-Cu-ZSM-5 catalysts, which were caused by excessive extra-framework Al and limitation in diffusion during Cu ion-exchange. Despite the strongest copper XPS peak intensity on the NR-Cu-ZSM-5 catalyst, the catalytic component is poorly dispersed due to too much CuO species existing on its surface. Combined with the  $\text{H}_2$ -TPR experiment on Con-Cu-ZSM-5 samples, the largest amount of CuO species in the bulk phase and the lowest XPS peak intensity essentially indicate that the Con-Cu-ZSM-5 zeolite is less suitable for dispersion with respect to the nanosheet samples. As shown in Table 2 and Fig.S1, compared to the Si/Al ratio determined by bulk phase (ICP) and framework (NMR), the surface Si/Al ratio of Con-Cu-ZSM-5 and NP-Cu-ZSM-5 samples is lower than the other samples, implying the occurrence of Al enrichment on the surface. Nevertheless, the surface Al-rich NP-Cu-ZSM-5 sample has no practical significance for the loading of copper ions because of the excessive amount of extra-framework Al species [the Si/Al ratio measured by ICP (19.2) and NMR (27.8) on NP-Cu-ZSM-5]. While for the  $\text{NS}_\text{L}$ -Cu-ZSM-5 and  $\text{NS}_\text{s}$ -Cu-ZSM-5 samples, the Si/Al ratios by XPS, ICP, and NMR are approximately the same, indicating that framework Al is uniformly distributed in the platelike nanosheet samples during the crystallization

Fig. 5. NH<sub>3</sub>-TPD profiles and NH<sub>3</sub> adsorption quantification of Cu-zeolite catalysts.Fig. 6. H<sub>2</sub>-TPR profiles and quantification of Cu species of the Cu-zeolite catalysts.

process along *a*-*c* orientation and most of the Si and Al atoms are well located in the skeleton.

EPR could be used to directly probe the amount of isolated Cu<sup>2+</sup> species and their fine structures in ZSM-5 zeolites owing to an unpaired

paramagnetic electron for isolated Cu<sup>2+</sup> ion. Isolated Cu<sup>2+</sup> species give a strong EPR response which can be detected at low temperatures, while silent to CuO<sub>x</sub> species and isolated Cu<sup>+</sup> ions [41,57]. As shown in Fig. 8, all Cu-ZSM-5 zeolites with different morphologies show the



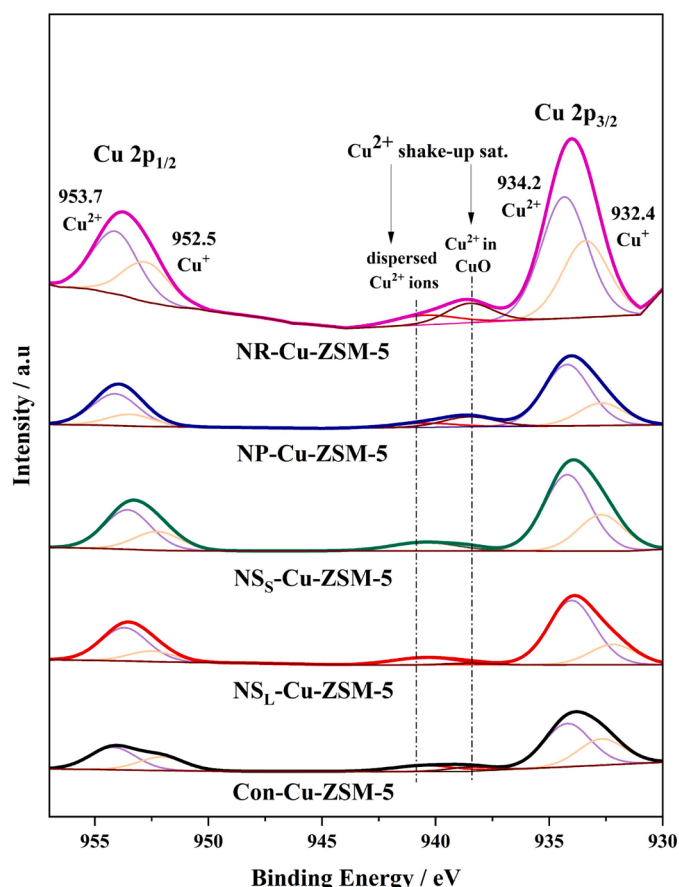


Fig. 7. XPS (Cu 2p) of copper ion-exchanged zeolites.

well-resolved hyperfine structures and the same  $g$  and  $A$  values ( $g_{\parallel} = 2.37$ ,  $g_{\perp} = 2.08$ , and  $A_{\parallel} = 136$  G), which suggests that the  $\text{Cu}^{2+}$  ions in the five catalysts are in tetragonally distorted octahedral coordination [58]. More importantly, the distribution of  $\text{Cu}^{2+}$  and  $[\text{Cu}(\text{OH})]^+$  species on Cu-ZSM-5 zeolites with different morphologies were accurately quantified by double integrating the dehydrated and hydrated EPR spectra [59]. After dehydration, EPR-active  $[\text{Cu}(\text{OH})]^+$  loses  $\text{H}_2\text{O}$  ligands and becomes EPR-silent due to a pseudo Jahn–Teller effect. Therefore, the signal loss of the dehydrated samples can be easily

calculated for quantifying the  $[\text{Cu}(\text{OH})]^+$  species. As shown in Fig.S2 and Table S7, the amount of  $\text{Cu}^{2+}$  and  $[\text{Cu}(\text{OH})]^+$  species is quantified by the EPR spectra over Cu-ZSM-5 catalysts. It is clear that the  $\text{Cu}^{2+}$  species dominate the majority of isolated  $\text{Cu}^{2+}$  ions in the NS<sub>L</sub>-Cu-ZSM-5 and NS<sub>S</sub>-Cu-ZSM-5 catalysts, while  $[\text{Cu}(\text{OH})]^+$  species accounts for the vast proportion of isolated  $\text{Cu}^{2+}$  ions over Con-Cu-ZSM-5 and NP-Cu-ZSM-5 zeolites. However, the dehydrated and hydrated EPR spectra of the NR-Cu-ZSM-5 catalyst were weaker than the others, demonstrating the presence of a large number of  $\text{CuO}_x$  clusters due to the silent EPR signal for  $\text{CuO}_x$  species.

As reported in the literatures [58,60], the most stable  $\text{Cu}^{2+}$  ions are readily located in the 6-MR, coordinated to three or four framework O atoms and balanced by paired negative framework charges. While the  $[\text{Cu}(\text{OH})]^+$  ions are commonly located at 10-MR, matching with two framework O atoms and one hydroxy O atom and balanced by single Al structure. Previous studies have further announced that the zeolite Si/Al ratio and metal loading method could affect the copper species, whereas it is herein important to note that the morphologies of zeolites indeed influence the distribution of copper species, including  $\text{Cu}^{2+}$  ions,  $[\text{Cu}(\text{OH})]^+$  ions, and  $\text{CuO}_x$  clusters [42,58].

### 3.3. XAS study

Copper, with its satisfactory redox properties and delicate coordinative flexibility, is closely related to an interaction with the crystal plane of the guest zeolite [61]. Fourier transform EXAFS spectra (Fig. 9a) were recorded in the range 0–4 Å to reveal the fine structure of copper species over five Cu-ZSM-5 zeolites with different morphologies. The EXAFS spectra of the copper reference samples were provided by the experiments (see Fig. 9b) and relevant literatures [61–64]. As illustrated in Fig. 9a, the R-space transformed EXAFS spectra of all samples were dominated by a Cu–O distance at  $\sim 1.5$  Å (peak  $\alpha$ ) [14,62,65]. In comparison with the reference Cu-species, the NS<sub>L</sub>-Cu-ZSM-5 and NS<sub>S</sub>-Cu-ZSM-5 catalysts could be fitted perfectly by the EXAFS spectra of  $[\text{Cu}(\text{II})(\text{H}_2\text{O})_6]^{2+}$ , so  $\text{Cu}^{2+}$  is the main copper species on the nanosheet zeolites. It is worth noting that no Cu–Cu (2.25 Å) and Cu–O–Cu (2.45 Å) coordination shells can be fitted by EXAFS results confirming the absence of copper oxides or Cu foil within broad Cu-ZSM-5 sheets. In addition, we suspect the nanosheet samples have only a small amount of  $[\text{Cu}(\text{OH})]^+$  species due to a partial overlap between  $[\text{Cu}(\text{II})(\text{H}_2\text{O})_6]^{2+}$  and  $[\text{Cu}(\text{OH})]^+$ . The EXAFS results corroborate the analysis of isolated  $\text{Cu}^{2+}$  ions by hydrated and dehydrated EPR spectra (Fig. 8 and Fig.S2), and no copper oxide species over nanosheets zeolites were further evidenced by the  $\text{H}_2$ -TPR (Fig. 6) and XPS data (Fig. 7). In contrast, for

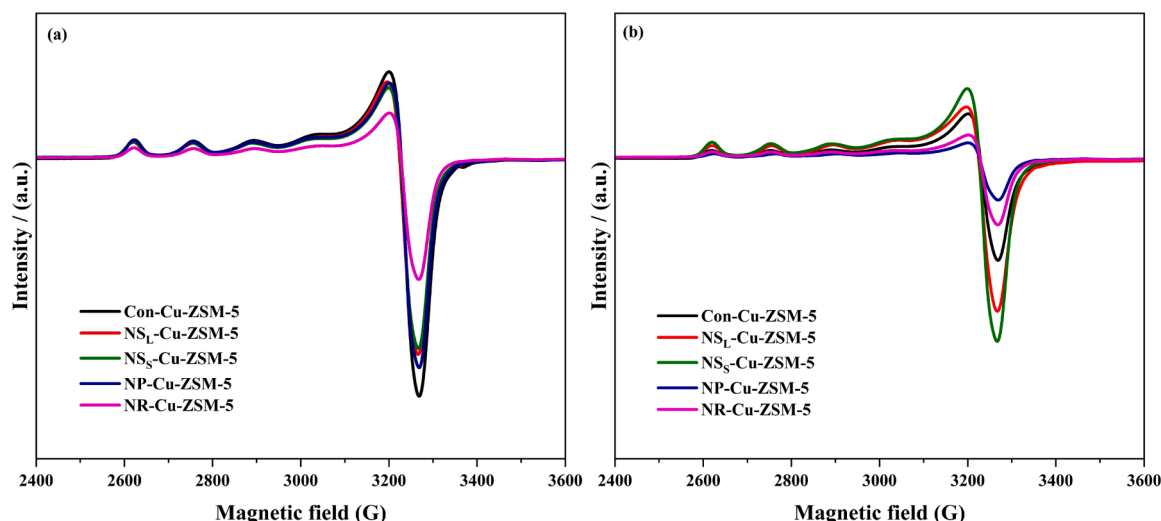


Fig. 8. EPR spectra of (a) hydrated, and (b) dehydrated Cu-ZSM-5 catalysts at 110 K.

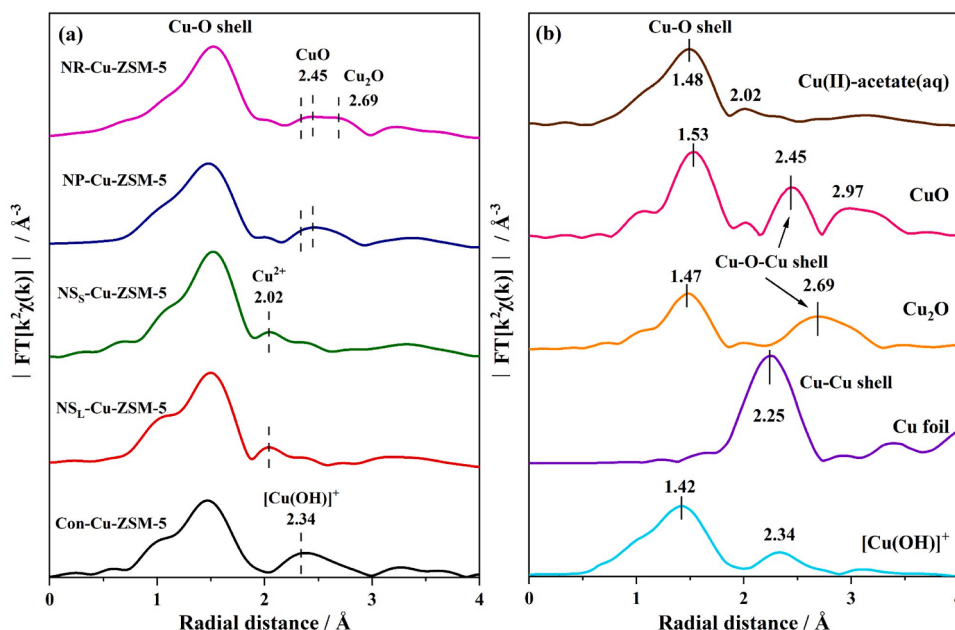


Fig. 9. The phase-uncorrected  $k^2$ -weighted FT EXAFS curves of a) Cu ion-exchange ZSM-5 zeolites with different morphologies and b) the copper reference samples.

non-nanosheet samples, there were no apparent curves that could be fitted by the  $[\text{Cu(II)(H}_2\text{O)}_6]^{2+}$  in  $[\text{Cu(II)-acetate(aq)}]$  standard, which were instead dominated by other standard samples, such as  $\text{CuO}$ ,  $\text{Cu}_2\text{O}$ , or  $[\text{Cu(OH)}]^+$ . The EXAFS spectra of the classical coffin-shaped Con-Cu-ZSM-5 zeolite can be fitted well by  $[\text{Cu(OH)}]^+$  species. The Cu-O-Cu (2.45 Å and 2.69 Å) shells can be fitted by the NP-Cu-ZSM-5 and NR-Cu-ZSM-5 catalysts, indicating that the copper oxide clusters are dominated on their surfaces. Too much copper oxide is caused by the inability of extra-framework Al to coordinate more copper ions on NP-Cu-ZSM-5 catalyst, while the large particle size of NR-Cu-ZSM-5 catalyst is not conducive to the exchange of more copper ions onto its Al sites in inner pore structure. Previous researchers have discovered the coordination number up to 6 for the first Cu-O shell in 100% exchanged Cu-ZSM-5 with Si/Al ratio of 25 [66]. The coordination number of our

as-prepared zeolite catalysts is around 1–1.4, speculating that we greatly preserve the Brønsted acid sites by sacrificing the amount of ion-exchanged Cu which are mainly balanced by hydroxyl groups for the reason of wide-temperature window for considerable activity. Furthermore, the Cu K-edge XANES curve was employed to differentiate the average valence state of copper species [67]. As shown in Fig.S3, the broad peak centered at  $\sim 9000.7$  eV corresponds to the average oxidation states of Cu species, suggesting the broad Cu-ZSM-5 sheets ( $\text{NS}_\text{L}$ -Cu-ZSM-5 and  $\text{NS}_\text{S}$ -Cu-ZSM-5) have a higher average valence state, and thus the nanosheet catalysts could promote more  $\text{Cu}^{2+}$  ions on the zeolitic support.

To further inspect the structure-composition-activity relationship of Cu-ZSM-5 zeolites at atomic level for achieving outstanding low-temperature  $\text{deNO}_\text{x}$  performance, the operando XAS in fluorescent

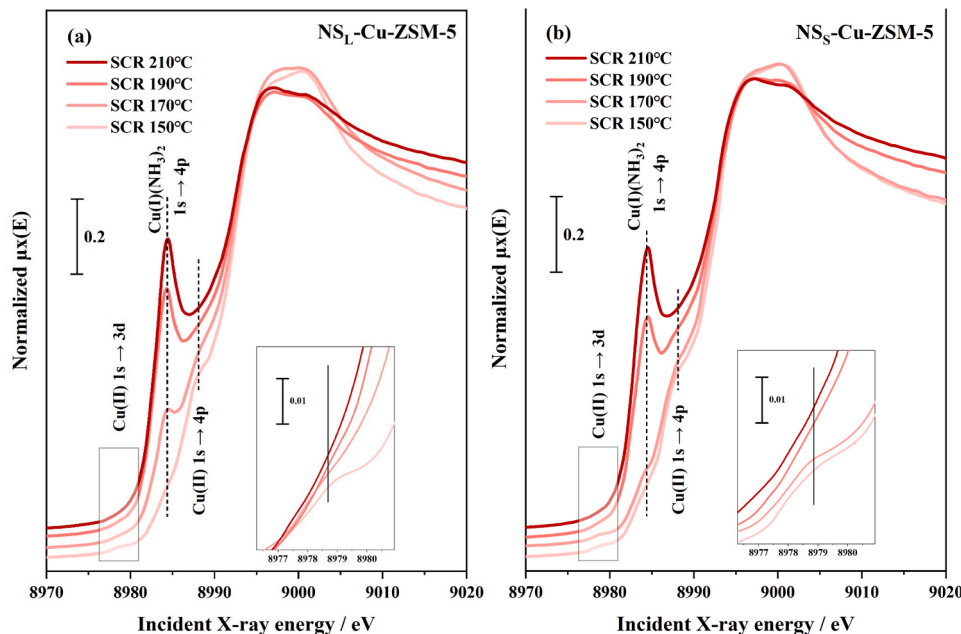


Fig. 10. Operando XANES collected during SCR process at temperatures of 150, 170, 190, and 210 °C. Insets report a magnification of the Cu(II) 1 s  $\rightarrow$  3d pre-edge peaks. (a)  $\text{NS}_\text{L}$ -Cu-ZSM-5 and (b)  $\text{NS}_\text{S}$ -Cu-ZSM-5.

pattern was used to monitor the atomic-scale behavior of the Cu species and their local coordination environments, oxidation states or valences with temperature shift gradually [62]. Fig. 10 shows the operando XANES spectra of NS<sub>L</sub>-Cu-ZSM-5 and NS<sub>S</sub>-Cu-ZSM-5 catalysts during low-temperature-dependent SCR process. As the temperature increases, the weak pre-edge peak at  $\sim 8977.7$  eV and the peak at  $\sim 8987.6$  eV are respectively assigned to the Cu<sup>2+</sup> 1s  $\rightarrow$  3d transition and the Cu<sup>2+</sup> 1s  $\rightarrow$  4p transition, both showing a slight increasing trend [68]. The intensity of the peak at  $\sim 9000.7$  eV from mobile and framework-interacting Cu species remain almost constant before 150 °C, however, the broad white line peak centered at  $\sim 9000.7$  eV shifts downwards with increasing temperature towards 170 °C, indicating a shift of the Cu<sup>2+</sup> sites to the average lower valence copper ions [61]. When the temperature reached 170 °C, the characteristic edge-rising peak at  $\sim 8984.3$  eV is attributed to 1s  $\rightarrow$  4p transition in Cu<sup>+</sup> exhibiting remarkable rise in intensity. The peak centered at  $\sim 8984.3$  eV represents a dynamic switch between Cu<sup>2+</sup> and Cu<sup>+</sup> during NH<sub>3</sub>-SCR reaction, demonstrating that redox cycling involving dynamic interconversion between NH<sub>3</sub>-solvated mononuclear Cu<sup>+</sup> and binuclear Cu<sup>2+</sup> complexes is critical for NH<sub>3</sub>-SCR process [14]. Compared to the other samples (Fig.S4), NS<sub>L</sub>-Cu-ZSM-5 catalyst showed a very pronounced and faster change in intensity of the change for each peak under operando condition and NS<sub>S</sub>-Cu-ZSM-5 catalyst followed closely, implying the rapid switch between Cu<sup>2+</sup> and Cu<sup>+</sup> in redox process. In addition, a weak peak fluctuation at  $\sim 8984.3$  eV can be observed in the in-situ XANES spectra (Fig.S5) collected during NH<sub>3</sub> adsorption at 100 °C, demonstrating that the Cu<sup>2+</sup> species were slowly reduced to Cu<sup>+</sup> in NH<sub>3</sub> stream [69]. This pre-reduction phenomenon is more apparent on NS<sub>L</sub>-Cu-ZSM-5 catalyst than the small nanosheet (NS<sub>S</sub>-Cu-ZSM-5) and other morphological zeolite catalysts at the same NH<sub>3</sub> absorption time (Fig.S5b). And in contrast to Fig. 10a, it can be seen that NO-O<sub>2</sub> played an important role in dynamic redox cycle in low temperature (so-called NO-activation cycle). In summary, the operando XANES spectra provide powerful evidence for NS<sub>L</sub>-Cu-ZSM-5 catalyst to exhibit an outstanding low-temperature SCR performance. On the one hand, the NH<sub>3</sub> adsorption acts as a pre-reduction process on the broad

Cu-ZSM-5 sheets to facilitate or activate the redox cycle, furthermore, the more rapid switch between Cu<sup>2+</sup> and Cu<sup>+</sup> species under NH<sub>3</sub>-SCR atmosphere [70].

The operando EXAFS provided a variation of the Cu coordination environment (Fig. 11). As shown in Fig. 11b, the first shell peak at 1.5 Å (peak  $\alpha$ ) in the NS<sub>L</sub>-Cu-ZSM-5 catalyst assigned to the Cu-O reference sample falls and then rises associated at the elevated temperatures, indicating that the copper species was initially reduced and subsequently oxidized, resulting in a switch between Cu<sup>2+</sup> and Cu<sup>+</sup>. At the same time, the Cu<sup>2+</sup> (peak  $\beta$ , 2.0 Å) species as key active sites only observed on the NS<sub>L</sub>-Cu-ZSM-5 catalyst were induced a visible shift of the peaks (peak  $\beta \rightarrow$  peak  $\gamma$ , 2.0 Å  $\rightarrow$  2.1 Å) in the range of 150–190 °C accompanied by its consumption and regeneration, which is assigned to the transformation of between Cu<sup>2+</sup> and Cu<sup>+</sup> [14]. In addition, the peak  $\eta$  (2.4 Å) corresponding to the Cu<sup>2+</sup>NO<sub>3</sub> reference can be detected on zeolites with other morphologies, and the peak at 3.2 Å is related to a multiple scattering characteristic to bidentate Cu<sup>2+</sup>NO<sub>3</sub> moieties, which displays the important reason for the superior low-temperature activity on NS<sub>L</sub>-Cu-ZSM-5 catalyst [71]. This is explained by the fact that the decomposition of HNNOH to H<sub>2</sub>O and N<sub>2</sub> is the rate-determining step of the NH<sub>3</sub>-SCR reaction. As far as the rapid switching of copper species in low-temperature region is concerned, the operando EXAFS results confirm that the rapid reduction of Cu<sup>2+</sup> to Cu<sup>+</sup> favors the NH<sub>3</sub>-SCR reaction.

### 3.4. DFT calculation

As the broad Cu-ZSM-5 sheets mainly exposed [010] crystal plane, in order to further illustrate the unique low-temperature effect of Cu<sup>2+</sup> ions and [010] crystal plane in the deNO<sub>x</sub> reaction, we carried out DFT calculations such as structure geometry optimization, transition states (TS) search, and densities of states (DOS) using the VASP to depict their potential energies and the electron transport properties. Fig. 12 shows the local structures and free energies of Cu-ZSM-5 zeolite and the TS energy barriers, which were calculated along the NH<sub>3</sub>-SCR pathways

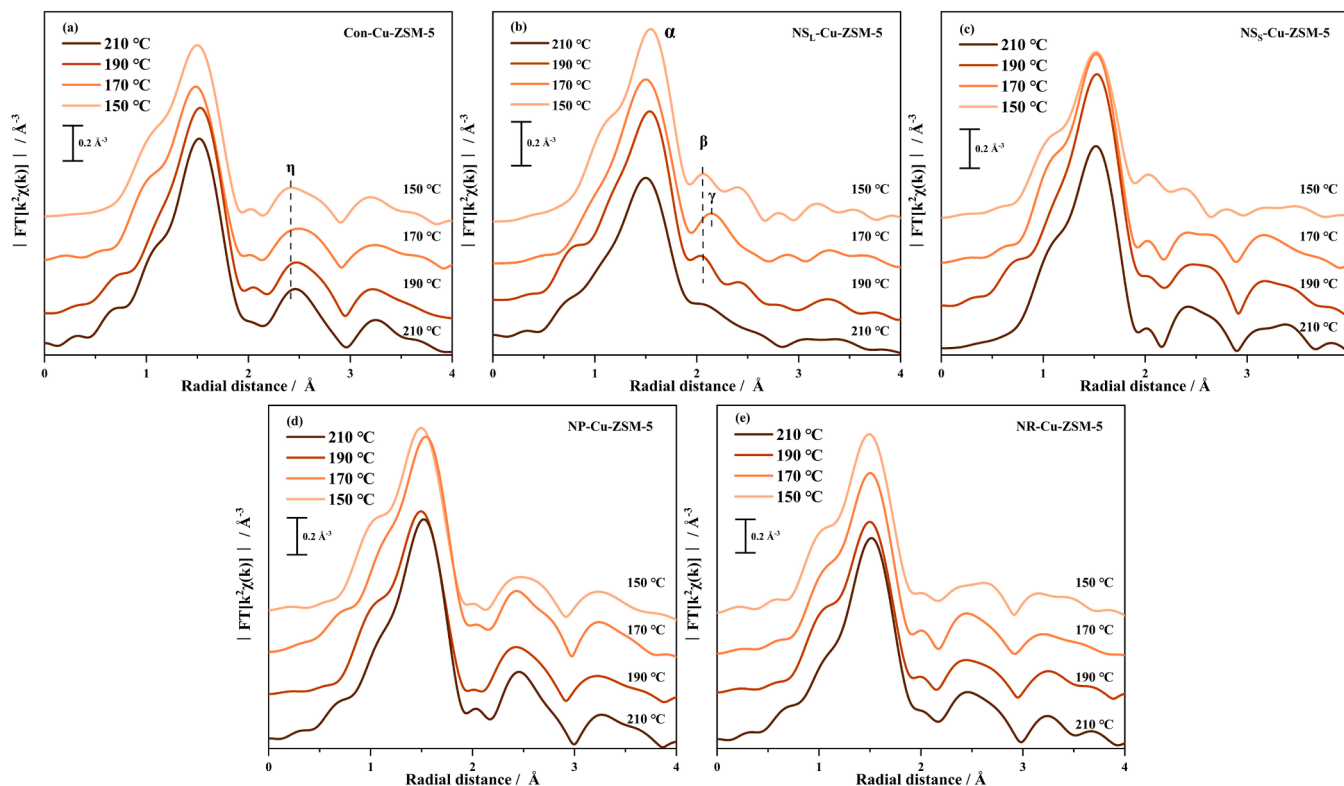


Fig. 11. The operando EXAFS spectra on Cu-ZSM-5 catalysts collected during SCR process at temperatures of 150, 170, 190, and 210 °C.



over different copper species and crystal planes, a complete redox cycle consists of  $\text{Cu}^{2+} \rightarrow \text{Cu}^+$  reduction half-cycle and  $\text{Cu}^+ \rightarrow \text{Cu}^{2+}$  re-oxidation half-cycle.

It is important to emphasize here to clarify that  $\text{Cu}^{2+}$  species with only one  $\text{NH}_3$  were regarded instead of the  $[\text{Cu}(\text{II})(\text{NH}_3)_4]^{2+}$  complexes, aiming to understand the effect of accurate van der Waals corrections on the energetics calculation of zeolite systems [72]. All active sites were established on 6-MR. The corresponding optimized geometries of all intermediates (IMs) and TSs are shown in Fig.S7 and specific information is illustrated in Table S8. The energy barrier ( $\Delta E$ ) of the rate-controlling step is summarized in Table S9.

According to previous reports by researchers, the adsorption of ammonia on copper species is more beneficial than nitric oxide, and the decomposition of  $\text{HNNOH}$  or  $\text{NO}_2/\text{NH}_4^+$  to  $\text{H}_2\text{O}$  and  $\text{N}_2$  (IM-5 to TS-1 and IM-10 to TS-2) is the rate-controlling step of the  $\text{NH}_3$ -SCR reaction [14, 66]. As shown in Fig. 12a, the NS-Cu-ZSM-5 catalyst with [010] crystal plane showed the lowest  $\Delta E$  (1.28 eV, 1.35 eV) in the formation of IM-5 to TS-1 and IM-10 to TS-2, respectively; while the  $\Delta E$  of [100] (1.61 eV, 1.61 eV) and [001] (1.82 eV, 1.85 eV) crystal planes showed rather high

energy barriers, which is kinetically unfavorable. The bond lengths of the intermediate species provide evidence as to why the [010] crystal plane showed the lowest energy barrier of the rate-controlling step. Table S10 shows the N-O bond lengths of IM-5 and IM-10, and it could be found that the intermediate species upon the [010] crystal plane shows the longest N-O bond lengths (IM-5 1.407 Å; IM-10 1.243 Å) among three crystal planes. The longer the bond length is, the easier its breakage becomes. In addition, the total densities of states (TDOS) and partial densities of states (PDOS) were calculated to further determination of the electron transport properties of  $\text{Cu}^{2+}$  ions on different crystal planes. As shown in Fig.S8, only the [010] crystal plane shows both the valence band (VB,  $-2 < E < 0$ ) and the conduction band (CB,  $0 < E < 3$ ), and the its Cu 3d orbitals have more contributions to the CB constitution as compared to [001] and [100] crystal planes. The VB was dominated by Si 2p, O 2p, and Cu 3d orbitals for [010] crystal plane, whereas the VB of [001] crystal plane has no contribution from Si 2p, indicating the bonded interaction among Si, O, and Cu atoms on [010] crystal plane. This suggests that the  $\text{Cu}^{2+}$  ions on [010] crystal plane have superior electron transport properties. As a result, the [010] crystal

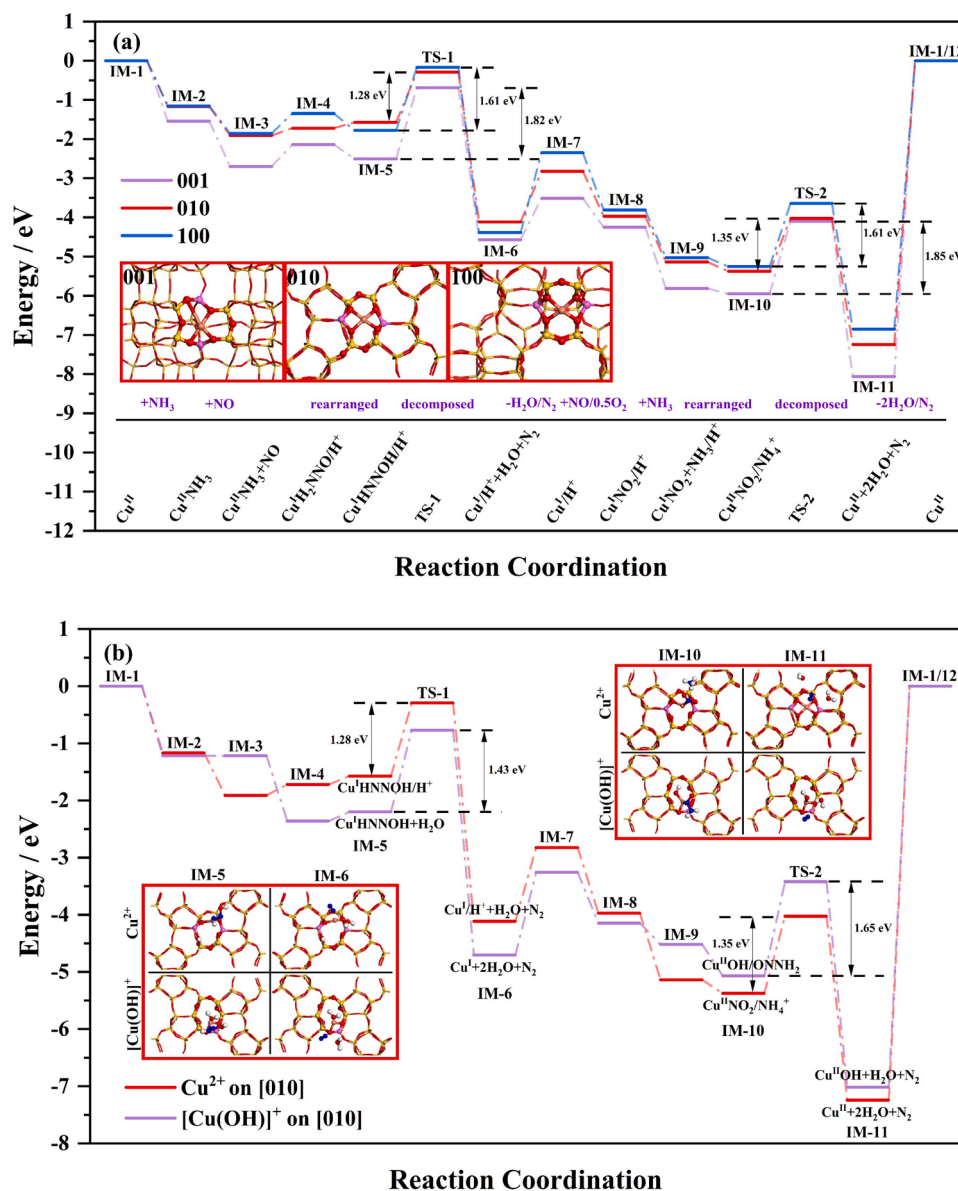


Fig. 12. Gibbs free energy profile result of  $\text{NH}_3$ -SCR redox pathways over (a) different crystal planes of Cu-ZSM-5: [001], [010], and [100]; (b)  $\text{Cu}^{2+}$  and  $[\text{Cu}(\text{OH})]^+$  on [010] crystal plane.

plane has the lowest energy barrier of the rate-controlling step than those of [001] and [100] crystal planes. Subsequently, the  $\Delta E$  of  $\text{Cu}^{2+}$  and  $[\text{Cu}(\text{OH})]^+$  were compared (Fig. 12b). The  $\Delta E$  (1.28 eV, 1.35 eV) in the formation of TS-1 and TS-2 on the  $\text{Cu}^{2+}$  upon [010] crystal plane is lower than those of  $[\text{Cu}(\text{OH})]^+$  (1.43 eV, 1.65 eV). Therefore, the DFT calculations demonstrated the  $\text{NS}_\text{L}$ -Cu-ZSM-5 catalyst with highly dispersed  $\text{Cu}^{2+}$  ions on the exposed [010] crystal plane has kinetic superiority in low-temperature  $\text{deNO}_x$ .

### 3.5. Catalytic activity and structure-performance relationship

Fig. 13a shows the  $\text{NH}_3$ -SCR activity of the Cu-ZSM-5 zeolites with different morphologies. The nanosheet and nanorod Cu-ZSM-5 zeolites with highly exposed  $b$ -axis direction exhibited much better performances than the classical coffin-shaped and nanoparticle ones, while the large nanosheet Cu-ZSM-5 catalyst showed the best low-temperature performance and the widest temperature window (250–550 °C) for  $\text{NO}_x$  removal. The activity order is of:  $\text{NS}_\text{L}$ -Cu-ZSM-5 >  $\text{NS}_\text{S}$ -Cu-ZSM-5 > NR-Cu-ZSM-5 > NP-Cu-ZSM-5 > Con-Cu-ZSM-5. In addition, as shown in Fig. 13b,  $\text{NO}$  can be completely converted into  $\text{N}_2$  at 250–550 °C for  $\text{NS}_\text{L}$ -Cu-ZSM-5 catalyst.

The excellent low-temperature redox capability of the broad Cu-ZSM-5 sheets is attributed to the following aspects. Firstly, the  $\text{NS}_\text{L}$ -Cu-ZSM-5 catalyst is only 20–40 nm in  $b$ -axis direction, which can extremely facilitate the dispersion of surface copper ions (0.73), as already revealed by  $\text{N}_2\text{O}$  chemisorption (Table 1). And its surface mesopores and internal micropores together construct hierarchically porous structure as the highway of mass transfer and diffusion for mobile hydrated copper species (i.e.  $[\text{Cu}(\text{II})(\text{H}_2\text{O})_6]^{2+}$ ,  $[\text{Cu}(\text{II})(\text{OH})(\text{H}_2\text{O})_5]^+$ ) and  $\text{NH}_3$ -solvated complexes (i.e.  $[\text{Cu}(\text{II})(\text{NH}_3)_4]^{2+}$ ,  $[\text{Cu}(\text{I})(\text{NH}_3)_2]^+$ ). Secondly, the operando XANES during  $\text{NH}_3$  adsorption revealed that  $\text{NS}_\text{L}$ -Cu-ZSM-5 catalyst could slowly reduce to  $\text{Cu}^+$  under ammonia atmosphere and such pre-reduction promotes low-temperature activity, because Cu species solvated by  $\text{NH}_3$  molecules are highly mobile. What's more, the lowest reduction temperature ( $\text{H}_2$ -TPR) and the most rapid switch between  $\text{Cu}^{2+}$  and  $\text{Cu}^+$  species (during operando XANES under  $\text{NH}_3$ -SCR atmosphere) demonstrated that  $\text{NS}_\text{L}$ -Cu-ZSM-5 catalyst has an outstanding low-temperature redox capability, which is inextricably linked to the distribution of Cu species and the specific interaction

between Cu species and zeolite crystal plane, especially  $\text{Cu}^{2+}$  ions and [010] facet. According to the DFT study (Fig. 12), the lowest  $\Delta E$  was obtained for highly dispersed  $\text{Cu}^{2+}$  ions on [010] crystal plane of ZSM-5 zeolite in the rate-determining step of  $\text{NH}_3$ -SCR. The Cu species distribution revealed by  $\text{H}_2$ -TPR, XPS, EPR, and EXAFS showed that the  $\text{NS}_\text{L}$ -Cu-ZSM-5 and  $\text{NS}_\text{S}$ -Cu-ZSM-5 catalysts were dominated by  $\text{Cu}^{2+}$  ions with small amounts of  $[\text{Cu}(\text{OH})]^+$  species and almost no  $\text{CuO}_x$  clusters. The NR-Cu-ZSM-5 catalyst with the highest Cu loading was dominated by  $\text{CuO}_x$  clusters, while its activity was inferior to those of the nanosheet zeolites and superior to those of the Con-Cu-ZSM-5 and NP-Cu-ZSM-5 catalysts, so the NR-Cu-ZSM-5 catalyst acted as a top-down sample indirectly demonstrated that the interaction of [010] crystal surface and  $\text{Cu}^{2+}$  ions is crucial for  $\text{NH}_3$ -SCR. In contrast, the Con-Cu-ZSM-5 and NP-Cu-ZSM-5 catalysts, no unique [010] crystal facet, have  $[\text{Cu}(\text{OH})]^+$  or  $\text{Cu}^{2+}$  species as the active sites, accompanied by a relatively large number of  $\text{CuO}_x$  clusters. The formation of  $\text{CuO}_x$  clusters was attributed to the interaction of  $\text{Cu}^{2+}$  ions with  $\text{O}^{2-}$  ions on the catalyst surface, although it was invisible by XRD technique (Fig. 1) likely due to its quite limited crystal domain. Owing to the large amount of extra-framework Al species, NP-Cu-ZSM-5 sample loaded with lower copper ions resulting in a relatively worse activity. As we all known, both  $\text{Cu}^{2+}$  and  $[\text{Cu}(\text{OH})]^+$  species are active sites in  $\text{NH}_3$ -SCR, but they presently show different catalytic performances. It was found that the nanosheet catalysts dominated by  $\text{Cu}^{2+}$  ions induced a rapid switching of copper species at low temperatures based on the operando XAS experiments. However, such phenomenon was hardly observed over the Con-Cu-ZSM-5 catalyst dominated by  $[\text{Cu}(\text{OH})]^+$  species. Furthermore, the DFT calculations provide a good explanation on the different activities of diverse copper species. Highly dispersed  $\text{Cu}^{2+}$  ions have lower energy barrier ( $\Delta E$ ) in the formation of TS in the rate-controlling step with respect to  $[\text{Cu}(\text{OH})]^+$  species. Therefore, we concluded that the broad nanosheet Cu-ZSM-5 firstly facilitated the distribution and dispersion of  $\text{Cu}^{2+}$  ions and enhanced the interaction with [010] crystal plane leading to a lowest energy barrier of the rate-determining step, and secondly enhanced the surface Brønsted acid sites and was prone to pre-reduction, leading to an outstanding low-temperature SCR activity.

As depicted in Fig. 13a, the  $\text{NS}_\text{L}$ -Cu-ZSM-5,  $\text{NS}_\text{S}$ -Cu-ZSM-5, and NR-Cu-ZSM-5 catalysts show excellent high-temperature  $\text{deNO}_x$  performances. It is quite interesting that the acid amounts of these nanosheet

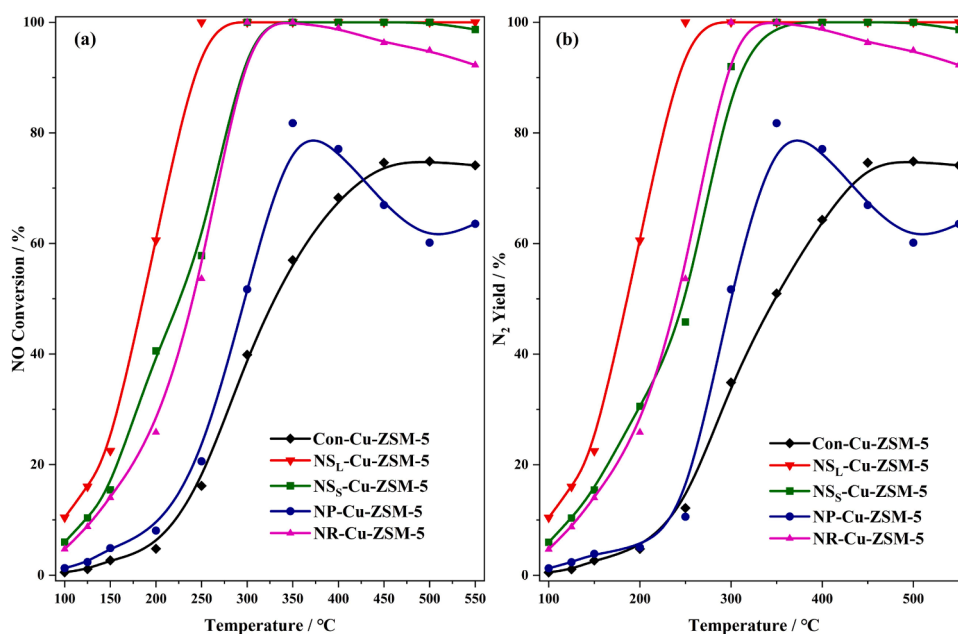


Fig. 13. Catalytic performance light-off curves over different zeolite catalysts: a)  $\text{NO}$  conversion and b)  $\text{N}_2$  yield. Conditions: 1000 ppm  $\text{NO}$ , 1000 ppm  $\text{NH}_3$ , 8 vol%  $\text{O}_2$ , 5 vol%  $\text{H}_2\text{O}$  balanced by  $\text{He}$ , gas hourly space velocity (GHSV) =  $\sim 50\,000\text{ h}^{-1}$ .

samples (NS<sub>L</sub>-Cu-ZSM-5 and NS<sub>S</sub>-Cu-ZSM-5) are not as much as that of NR-Cu-ZSM-5 catalyst, but they show superior SCR activity at high temperatures, which is likely attributed to not only the contribution of Brønsted acid sites (Fig. 5) but also their excellent BET surface areas and high dispersion of copper species. Although the dispersion of copper species of NR-Cu-ZSM-5 catalyst is not satisfactory, it has the most abundant acid sites owing to the lowest Si/Al ratio. As expected, the NP-Cu-ZSM-5 catalyst shows a rather poor high-temperature activity, because its extra-framework Al resulted in unsatisfactory acid strength to adsorb NH<sub>3</sub> molecules weakly. The Brønsted acid sites play an important role in the high-temperature NH<sub>3</sub>-SCR reaction according to the literature [42,47,73–75]. The Brønsted acid sites are verified by Pyridine-IR study (Fig.S9) to interact strongly with NH<sub>3</sub>, which make the adsorbed NH<sub>3</sub> more stable, thereby inhibiting the progress of hostile side reactions of ammonia oxidation, and consequently promote the high-temperature SCR activity.

In order to clarify the reaction rate of five Cu-ZSM-5 zeolites and their catalytic ability of each copper site, Fig.S6 shows the kinetic tests (Arrhenius plots and turnover frequency) of catalysts were measured in low-conversion zone (<30%). Among these catalysts, the NS<sub>L</sub>-Cu-ZSM-5 catalyst exhibited the lowest activation energy (~23.94 kJ/mol) and the highest turnover frequency and followed by NS<sub>S</sub>-Cu-ZSM-5 one, implying that each copper site on NS<sub>L</sub>-Cu-ZSM-5 catalyst was more valid for NH<sub>3</sub>-SCR process.

The tolerance of H<sub>2</sub>O and SO<sub>2</sub> is crucial for practical applications [76,77]. The tolerance experiments of H<sub>2</sub>O and SO<sub>2</sub> on Cu-ZSM-5 with diverse morphologies were performed (Fig.S10). The NS<sub>L</sub>-Cu-ZSM-5 catalyst showed the excellent resistance towards H<sub>2</sub>O poisoning and maintained 100% NO conversion under humidity for 8 h during the NH<sub>3</sub>-SCR process. However, the other catalysts presented various degrees of activity decrease in terms of steam existence. Fortunately, when cut off 10% water vapor, the activities of NS<sub>S</sub>-Cu-ZSM-5 and NR-Cu-ZSM-5 were fully restored up to 100%. Next, all zeolites with diverse morphologies were deactivated by 15–25% after being exposed to 200 ppm SO<sub>2</sub> for 8 h. All catalysts, except for NS<sub>L</sub>-Cu-ZSM-5, could not be recovered after removing the SO<sub>2</sub>. Ultimately, all catalysts significantly reduced the corresponding NO conversion along with H<sub>2</sub>O and SO<sub>2</sub> poisoning.

#### 4. Conclusions

In summary, outstanding low-temperature deNO<sub>x</sub> was achieved by designing copper-based ZSM-5 zeolite with broad sheet characteristic and highly exposed *a*-c orientation. The NS<sub>L</sub>-Cu-ZSM-5 catalysts showed excellent low-temperature performance while keeping high-temperature activity, achieving complete deNO<sub>x</sub> at 250–550 °C. Compared to the conventional and nanoparticle Cu-ZSM-5 zeolites, the broad Cu-ZSM-5 sheets have short straight channels for rapid mass transfer and diffusion, as well as more widely distributed surface acidity and highly dispersed copper species. The large nanosheet Cu-ZSM-5 catalyst without copper oxide clusters has highly dispersed Cu<sup>2+</sup> ions as the main active sites of deNO<sub>x</sub>, which was revealed by EPR and EXAFS experiments. As demonstrated by operando XAS experiments, the broad Cu-ZSM-5 catalyst with highly exposed [010] crystal plane is more beneficial for promoting the pre-reduction of copper species during ammonia adsorption (Cu<sup>2+</sup> → Cu<sup>+</sup>), and the Cu<sup>2+</sup> species as key active sites and the [010] crystal plane together constitute an unique and efficient low-temperature active site to facilitate the dynamic switch between [Cu(II)(NH<sub>3</sub>)<sub>4</sub>]<sup>2+</sup> and [Cu(I)(NH<sub>3</sub>)<sub>2</sub>]<sup>+</sup> complexes (Cu<sup>2+</sup> ↔ Cu<sup>+</sup>). Finally, the DFT calculations verified that the Cu<sup>2+</sup> ions over [010] crystal plane of ZSM-5 zeolite effectively lowered the reaction energy barrier of the SCR rate-controlling step (i.e. [Cu(I)HNOH]<sup>+</sup>/H<sup>+</sup> → [Cu(I)]<sup>+</sup>/H<sup>+</sup> + H<sub>2</sub>O + N<sub>2</sub>).

#### CRedit authorship contribution statement

**Xiaonan Guo:** Conceptualization, Investigation, Methodology, Writing – original draft, Validation. **Runduo Zhang:** Supervision, Writing – review & editing, Funding acquisition. **Zhaoying Di:** Investigation, Formal analysis, Methodology. **Bin Kang:** Data curation. **Hanxiao Shen:** Investigation. **Ying Wei:** Formal analysis, Project administration. **Jingbo Jia:** Visualization, Methodology. **Lirong Zheng:** Methodology.

#### Declaration of Competing Interest

The authors declare that they have no known competing financial interests or personal relationships that could have appeared to influence the work reported in this paper.

#### Data Availability

Data will be made available on request.

#### Acknowledgments

This work was supported by the National Natural Science Foundation of China (Nos. 22176010 and 21976012) and Innovation Fund of SINOPEC Catalyst Co. Ltd-State Key Laboratory of Chemical Resource Engineering (No. 36100000-22-ZC0607-0041).

#### Appendix A. Supporting information

Supplementary data associated with this article can be found in the online version at doi:10.1016/j.apcatb.2023.123519.

#### References

- [1] R. Carmona-Cabezas, J. Gómez-Gómez, E.G.D. Ravé, E. Sánchez-López, J. Serrano, F.J. Jiménez-Hornero, Improving graph-based detection of singular events for photochemical smog agents, *Chemosphere* 253 (2020), 126660, <https://doi.org/10.1016/j.chemosphere.2020.126660>.
- [2] Y. Xie, H.C. Dai, Y.X. Zhang, Y.Z. Wu, T. Hanaoka, T. Masui, Comparison of health and economic impacts of PM<sub>2.5</sub> and ozone pollution in China, *Environ. Int.* 130 (2019), 104881, <https://doi.org/10.1016/j.envint.2019.05.075>.
- [3] M. Stafoggia, B. Oftedal, J. Chen, et al., Long-term exposure to low ambient air pollution concentrations and mortality among 28 million people: results from seven large European cohorts within the ELAPSE project, *Lancet Planet. Health* 6 (2022) 9–18, [https://doi.org/10.1016/S2542-5196\(21\)00277-1](https://doi.org/10.1016/S2542-5196(21)00277-1).
- [4] W. Song, X.Y. Liu, C.C. Hu, G.Y. Chen, X.J. Liu, W.W. Walters, G. Michalski, C. Q. Liu, Important contributions of non-fossil fuel nitrogen oxides emissions, *Nat. Commun.* 12 (2021) 243–249, <https://doi.org/10.1038/s41467-020-20356-0>.
- [5] Z.M. Liu, J.H. Li, S.I. Woo, Recent advances in the selective catalytic reduction of NO<sub>x</sub> by hydrogen in the presence of oxygen, *Energy Environ. Sci.* 5 (2012) 8799–8814, <https://doi.org/10.1039/c2ee22190j>.
- [6] Y.L. Shan, J.P. Du, Y. Zhang, W.P. Shan, X.Y. Shi, Y.B. Yu, R.D. Zhang, X.J. Meng, F. S. Xiao, H. He, Selective catalytic reduction of NO<sub>x</sub> with NH<sub>3</sub>: opportunities and challenges of Cu-based small-pore zeolites, *Natl. Sci. Rev.* 8 (2021) 1–20, <https://doi.org/10.1093/nsr/nwab010>.
- [7] E.M. Elliott, C. Kendall, S.D. Wankel, D.A. Burns, E.W. Boyer, K. Harlin, D.J. Bain, T.J. Butler, Nitrogen isotopes as indicators of NO<sub>x</sub> source contributions to atmospheric nitrate deposition across the midwestern and northeastern united states, *Environ. Sci. Technol.* 41 (2007) 7661–7667, <https://doi.org/10.1021/es070898t>.
- [8] W. Zheng, J.L. Chen, L. Guo, W.B. Zhang, H.R. Zhao, X.Q. Wu, Research progress of hydrothermal stability of metal-based zeolite catalysts in NH<sub>3</sub>-SCR reaction, *J. Fuel Chem. Technol.* 48 (2020) 1193–1210, [https://doi.org/10.1016/S1872-5813\(20\)30081-5](https://doi.org/10.1016/S1872-5813(20)30081-5).
- [9] Y.G. Zhao, J. Hu, L. Hua, S.J. Shuai, J.X. Wang, Ammonia storage and slip in a urea selective catalytic reduction catalyst under steady and transient conditions, *Ind. Eng. Chem. Res.* 50 (2011) 11863–11871, <https://doi.org/10.1021/ie201045w>.
- [10] Y.J. Pu, X.Y. Xie, W.J. Jiang, L. Yang, X. Jiang, L. Yao, Low-temperature selective catalytic reduction of NO<sub>x</sub> with NH<sub>3</sub> over zeolite catalysts: a review, *Chin. Chem. Lett.* 31 (2020) 2549–2555, <https://doi.org/10.1016/j.ccl.2020.04.012>.
- [11] M.F. Fu, C.T. Li, P. Lu, L. Qu, M.Y. Zhang, Y. Zhou, M.G. Yu, Y. Fang, A review on selective catalytic reduction of NO<sub>x</sub> by supported catalysts at 100–300 °C - catalysts, mechanism, kinetics, *Catal. Sci. Technol.* 1 (2014) 14–25, <https://doi.org/10.1039/c3cy00414g>.
- [12] J.H. Li, H.Z. Chang, L. Ma, J.M. Hao, R.T. Yang, Low-temperature selective catalytic reduction of NO<sub>x</sub> with NH<sub>3</sub> over metal oxide and zeolite catalysts - a



- review, *Catal. Today* 175 (2011) 147–156, <https://doi.org/10.1016/j.cattod.2011.03.034>.
- [13] S.G. Zhang, B.L. Zhang, B. Liu, S.L. Sun, A review of Mn-containing oxide catalysts for low temperature selective catalytic reduction of NO<sub>x</sub> with NH<sub>3</sub>: reaction mechanism and catalyst deactivation, *RSC Adv.* 7 (2017) 26226–26242, <https://doi.org/10.1039/c7ra03387g>.
- [14] H. Wang, J.B. Jia, S.S. Liu, H.X. Chen, Y. Wei, Z.J. Wang, L.R. Zheng, Z.C. Wang, R. D. Zhang, Highly efficient NO abatement over Cu-ZSM-5 with special nanosheet features, *Environ. Sci. Technol.* 55 (2021) 5422–5434, <https://doi.org/10.1021/acs.est.0c08684>.
- [15] H. Dai, Y.F. Shen, T.M. Yang, C.S. Lee, D.L. Fu, A. Agarwal, T.T. Le, M. Tsapatsis, J. C. Palmer, B.M. Weckhuysen, P.J. Dauenhauer, X.D. Zou, J.D. Rimer, Finned zeolite catalysts, *Nat. Mater.* 19 (2020) 1074–1080, <https://doi.org/10.1038/s41563-020-0753-1>.
- [16] N. Wang, Q.M. Sun, T.J. Zhang, A. Mayoral, L. Li, X. Zhou, J. Xu, P. Zhang, J.H. Yu, Impregnating subnanometer metallic nanocatalysts into self-pillared zeolite nanosheets, *J. Am. Chem. Soc.* 143 (2021) 6905–6914, <https://doi.org/10.1021/jacs.1c00578>.
- [17] H. Wang, R.N. Xu, Y. Jin, R.D. Zhang, Zeolite structure effects on Cu active center, SCR performance and stability of Cu-zeolite catalysts, *Catal. Today* 327 (2019) 295–307, <https://doi.org/10.1016/j.cattod.2018.04.035>.
- [18] C. Peng, R. Yan, H.G. Peng, Y.Y. Mi, J. Liang, W.M. Liu, X. Wang, G. Song, P. Wu, F. D. Liu, One-pot synthesis of layered mesoporous ZSM-5 plus Cu ion-exchange: Enhanced NH<sub>3</sub>-SCR performance on Cu-ZSM-5 with hierarchical pore structures, *J. Hazard. Mater.* 385 (2020), 121593, <https://doi.org/10.1016/j.jhazmat.2019.121593>.
- [19] Y. Ma, X.M. Tang, J.Y. Hu, Y.H. Ma, W. Chen, Z.Q. Liu, S.C. Han, C. Xu, Q.M. Wu, A.M. Zhang, L.F. Zhu, X.J. Meng, F.S. Xiao, Design of a small organic template for the synthesis of self-pillared pentasil zeolite nanosheets, *J. Am. Chem. Soc.* 144 (2022) 6270–6277, <https://doi.org/10.1021/jacs.1c12338>.
- [20] W.J. Dai, C. Kouvatias, W.S. Tai, G.J. Wu, N.J. Guan, L.D. Li, V. Valtchev, Platelike MFI crystals with controlled crystal faces aspect ratio, *J. Am. Chem. Soc.* 143 (2021) 1993–2004, <https://doi.org/10.1021/jacs.0c11784>.
- [21] J.X. Zhang, L.M. Ren, A.J. Zhou, W.H. Li, S.J. Shang, Y. Liu, Z.H. Jia, W. Liu, A. F. Zhang, X.W. Guo, Tailored synthesis of ZSM-5 nanosheets with controllable *b*-axis thickness and aspect ratio: strategy and growth mechanism, *Chem. Mater.* 34 (2022) 3217–3226, <https://doi.org/10.1021/acs.chemmater.2c00001>.
- [22] Z.G. Hou, X.T. Mi, X.G. Li, H.T. Liu, Seed-assisted synthesis of ZSM-5 aggregates assembled from regularly stacked nanosheets and their performance in *n*-Hexane aromatization, *Ind. Eng. Chem. Res.* 60 (2021) 12100–12108, <https://doi.org/10.1021/acs.iecr.1c01894>.
- [23] J.D. Duan, W. Chen, C.T. Wang, L. Wang, Z.Q. Liu, X.F. Yi, W. Fang, H. Wang, H. Wei, S.D. Xu, Y.W. Yang, Q.W. Yang, Z.B. Bao, Z.G. Zhang, Q.L. Ren, H. Zhou, X. D. Qin, A.M. Zheng, F.S. Xiao, Coking-resistant polyethylene upcycling modulated by zeolite micropore diffusion, *J. Am. Chem. Soc.* 144 (2022) 14269–14277, <https://doi.org/10.1021/jacs.2c05125>.
- [24] Y.F. Shen, T.T. Le, D.L. Fu, J.E. Schmidt, M. Filez, B.M. Weckhuysen, J.D. Rimer, Deconvoluting the competing effects of zeolite framework topology and diffusion path length on methanol to hydrocarbons reaction, *ACS Catal.* 8 (2018) 11042–11053, <https://doi.org/10.1021/acscatal.8b02274>.
- [25] M. Firoozi, M. Baghalha, M. Asadi, The effect of micro and nano particle sizes of H-ZSM-5 on the selectivity of MTP reaction, *Catal. Commun.* 10 (2009) 1582–1585, <https://doi.org/10.1016/j.catcom.2009.04.021>.
- [26] G. Kresse, J. Hafner, Ab initio molecular dynamics for open-shell transition metals, *Phys. Rev. B* 48 (1993) 13115, <https://doi.org/10.1103/PhysRevB.48.13115>.
- [27] Y.W. Zhang, J.Y. Yu, Y.H. Yeh, R.J. Gorte, S. Rangarajan, M. Mavrikakis, An adsorption study of CH<sub>4</sub> on ZSM-5, MOR, and ZSM-12 zeolites, *J. Phys. Chem. C* 119 (2015) 28970–28978, <https://doi.org/10.1021/acs.jpcc.5b09571>.
- [28] G. Kresse, D. Joubert, From ultrasoft pseudopotentials to the projector augmented-wave method, *Phys. Rev. B* 59 (1999) 1758, <https://doi.org/10.1103/PhysRevB.59.1758>.
- [29] J.P. Perdew, K. Burke, M. Ernzerhof, Generalized gradient approximation made simple, *Phys. Rev. Lett.* 77 (1996) 3865, <https://doi.org/10.1103/PhysRevLett.77.3865>.
- [30] W.Y. Song, J. Liu, H.L. Zheng, S.C. Ma, Y.C. Wei, A.J. Duan, G.Y. Jiang, Z. Zhao, E. J.M. Hensen, A mechanistic DFT study of low temperature SCR of NO with NH<sub>3</sub> on MnCe<sub>1-x</sub>O<sub>2</sub>(111), *Catal. Sci. Technol.* 6 (2016) 2120–2128, <https://doi.org/10.1039/c5cy01597a>.
- [31] L.Q. Meng, X.C. Zhu, E.J.M. Hensen, Stable Fe/ZSM-5 nanosheet zeolite catalysts for the oxidation of benzene to phenol, *ACS Catal.* 7 (2017) 2709–2719, <https://doi.org/10.1021/acscatal.6b03512>.
- [32] X.L. Shao, S.Q. Wang, Y.H. Zhou, X. Zhang, H.Z. Tian, Z. Wang, Z.Y. Yuan, H. T. Wang, Synthesis of multilamellar ZSM-5 nanosheets with tailored *b*-axis thickness, *Microporous Mesoporous Mater.* 345 (2022), 112252, <https://doi.org/10.1016/j.micromeso.2022.112252>.
- [33] W. Song, R.E. Justice, C.A. Jones, V.H. Grassian, S.C. Larsen, Synthesis, characterization, and adsorption properties of nanocrystalline ZSM-5, *Langmuir* 20 (2004) 8301–8306, <https://doi.org/10.1021/la049516c>.
- [34] E.S. Zhan, Z.P. Xiong, Y. Zhou, M.R. Li, P.F. Wang, W.B. Fan, W.J. Shen, Perpendicular intergrowth ZSM-5 plates with shortened 10-MR pores, *Chin. J. Catal.* 14 (2020) 1132–1139, [https://doi.org/10.1016/S1872-2067\(20\)63573-2](https://doi.org/10.1016/S1872-2067(20)63573-2).
- [35] Q.Y. Wu, M.R. Li, Y. Huang, Y.M. Fang, Hierarchical ZSM-5 by 90° twin intergrowth of mesoporous nanofibers: synthesis and application in methanol/propanol to hydrocarbon reaction, *Microporous Mesoporous Mater.* 226 (2016) 284–291, <https://doi.org/10.1016/j.micromeso.2016.02.002>.
- [36] D.P. Serrano, J.M. Escalac, P. Pizarroa, Synthesis strategies in the search for hierarchical zeolites, *Chem. Soc. Rev.* 42 (2013) 4004–4035, <https://doi.org/10.1039/c2cs35330j>.
- [37] T. Wakihara, A. Ihara, S. Inagaki, J. Tatami, K. Sato, K. Komeya, T. Meguro, Y. Kubota, A. Nakahira, Top-down tuning of nanosized ZSM-5 zeolite catalyst by bead milling and recrystallization, *Cryst. Growth Des.* 11 (2011) 5153–5158, <https://doi.org/10.1021/cg201078r>.
- [38] S. Sen, R.R. Wusirika, R.E. Youngman, High temperature thermal expansion behavior of H[Al]ZSM-5 zeolites: The role of Brønsted sites, *Microporous Mesoporous Mater.* 87 (2006) 217–223, <https://doi.org/10.1016/j.micromeso.2005.08.010>.
- [39] P. Szazama, B. Wichterlova, J. Dedeczek, Z. Tvaruzkova, Z. Musilova, L. Palumbo, S. Sklenak, O. Gonsiorova, FTIR and <sup>27</sup>Al MAS NMR analysis of the effect of framework Al- and Si-defects in micro- and micro-mesoporous H-ZSM-5 on conversion of methanol to hydrocarbons, *Microporous Mesoporous Mater.* 143 (2011) 87–96, <https://doi.org/10.1016/j.micromeso.2011.02.013>.
- [40] O.H. Han, C.S. Kim, S.B. Hong, Direct evidence for the nonrandom nature of Al substitution in zeolite ZSM-5: an investigation by <sup>27</sup>Al MAS and MQ MAS NMR, *Angew. Chem.* 41 (2002) 469–472, [https://doi.org/10.1002/1521-3773\(20020201\)41:3<469::AID-ANGE469>3.0.CO;2-K](https://doi.org/10.1002/1521-3773(20020201)41:3<469::AID-ANGE469>3.0.CO;2-K).
- [41] Y.N. Zhang, H.C. Zhu, T. Zhang, J. Li, J.J. Chen, Y. Peng, J.H. Li, Revealing the synergistic deactivation mechanism of hydrothermal aging and SO<sub>2</sub> poisoning on Cu/SSZ-13 under SCR condition, *Environ. Sci. Technol.* 56 (2022) 1917–1926, <https://doi.org/10.1021/acs.est.1c06068>.
- [42] F. Gao, N.M. Washton, Y.L. Wang, M. Kollár, J. Szanyi, C.H.F. Peden, Effects of Si/Al ratio on Cu/SSZ-13 NH<sub>3</sub>-SCR catalysts: Implications for the active Cu species and the roles of Brønsted acidity, *J. Catal.* 331 (2015) 25–38, <https://doi.org/10.1016/j.jcat.2015.08.004>.
- [43] S.S.R. Putluru, A. Riisager, R. Fehrmann, Alkali resistant Cu/zeolite deNO<sub>x</sub> catalysts for flue gas cleaning in biomass fired applications, *Appl. Catal. B: Environ.* 101 (2011) 183–188, <https://doi.org/10.1016/j.apcatb.2010.09.015>.
- [44] Z. Chen, C. Fan, L. Pang, S.J. Ming, P. Liu, T. Li, The influence of phosphorus on the catalytic properties, durability, sulfur resistance and kinetics of Cu-SSZ-13 for NO<sub>x</sub> reduction by NH<sub>3</sub>-SCR, *Appl. Catal. B: Environ.* 237 (2018) 116–127, <https://doi.org/10.1016/j.apcatb.2018.05.075>.
- [45] T. Zhang, F. Qiu, J.H. Li, Design and synthesis of core-shell structured meso-Cu-SSZ-13@mesoporous aluminosilicate catalyst for SCR of NO<sub>x</sub> with NH<sub>3</sub>: Enhancement of activity, hydrothermal stability and propene poisoning resistance, *Appl. Catal. B: Environ.* 237 (2016) 48–58, <https://doi.org/10.1016/j.apcatb.2016.04.058>.
- [46] D. Yu, P. Wang, X.J. Li, H.Y. Zhao, X.L. Lv, Study on the role of Fe species and acid sites in NH<sub>3</sub>-SCR over the Fe-based zeolites, *Fuel* 336 (2023), 126759, <https://doi.org/10.1016/j.fuel.2022.126759>.
- [47] L. Wang, W. Li, S.J. Schmieg, D. Weng, Role of Brønsted acidity in NH<sub>3</sub> selective catalytic reduction reaction on Cu/SAPO-34 catalysts, *J. Catal.* 324 (2015) 98–106, <https://doi.org/10.1016/j.jcat.2015.01.011>.
- [48] E.H. Yuan, M. Li, M.H. Yang, X.S. Huang, K. Zhang, W.L. Han, Z.C. Tang, Z.W. Liu, Encapsulation of ultra-small Cu-Fe into ZSM-5 zeolites for NH<sub>3</sub>-SCR with broad reaction-temperature ranges, *Microporous Mesoporous Mater.* 331 (2022), 111675, <https://doi.org/10.1016/j.micromeso.2021.111675>.
- [49] Z.C. Wang, S. Pokhrel, M.M. Chen, M. Hunger, L. Mädler, J. Huang, Palladium-doped silica–alumina catalysts obtained from double-flame FSP for chemoselective hydrogenation of the model aromatic ketone acetophenone, *J. Catal.* 302 (2013) 10–19, <https://doi.org/10.1016/j.jcat.2013.02.017>.
- [50] C. Peng, J. Liang, H.G. Peng, R. Yan, W.M. Liu, Z. Wang, P. Wu, X. Wang, Design and synthesis of Cu/ZSM-5 catalyst via a facile one-pot dual-template strategy with controllable Cu content for removal of NO<sub>x</sub>, *Ind. Eng. Chem. Res.* 57 (2018) 14967–14976, <https://doi.org/10.1021/acs.iecr.8b03432>.
- [51] B.E.R. Snyder, M.L. Bols, R.A. Schoonheydt, B.F. Sels, E.I. Solomon, Iron and copper active sites in zeolites and their correlation to metalloenzymes, *Chem. Rev.* 118 (2018) 2718–2768, <https://doi.org/10.1021/acs.chemrev.7b00344>.
- [52] M. Jablonka, K. Góra-Marek, P.C. Bruzzese, A. Palčić, K. Pyra, K. Tarach, M. Bertmer, D. Poppitz, A. Pöpl, R. Gläser, Influence of framework n(Si)/n(Al) ratio on the nature of Cu species in Cu-ZSM-5 for NH<sub>3</sub>-SCR-DeNO<sub>x</sub>, *ChemCatChem* 14 (2022) 1–14, <https://doi.org/10.1002/cctc.202200627>.
- [53] M. Lei, N. Wang, L.H. Zhu, Q.L. Zhou, G. Nie, H.Q. Tang, Photocatalytic reductive degradation of polybrominated diphenyl ethers on CuO/TiO<sub>2</sub> nanocomposites: A mechanism based on the switching of photocatalytic reduction potential being controlled by the valence state of copper, *Appl. Catal. B: Environ.* 182 (2016) 414–423, <https://doi.org/10.1016/j.apcatb.2015.09.031>.
- [54] Z.G. Li, X.Y. Chen, J.H. Li, X.N. Ren, S.X. Liu, J.D. Gao, J.W. Schwank, T. Zhang, W. K. Su, H.Z. Chang, Synthesis and evaluation of mesopore structured ZSM-5 and a CuZSM-5 catalyst for NH<sub>3</sub>-SCR reaction: studies of simulated exhaust and engine bench testing, *RSC Adv.* 6 (2016) 102570–102581, <https://doi.org/10.1039/c6ra22373c>.
- [55] B.J. Dou, G. Lv, C. Wang, Q.L. Hao, K.S. Hui, Cerium doped copper/ZSM-5 catalysts used for the selective catalytic reduction of nitrogen oxide with ammonia, *Chem. Eng. J.* 270 (2015) 549–556, <https://doi.org/10.1016/j.cej.2015.02.004>.
- [56] R.D. Zhang, W.Y. Teoh, R. Amal, B.H. Chen, S. Kaliaguine, Catalytic reduction of NO by CO over Cu/Ce<sub>x</sub>Zr<sub>1-x</sub>O<sub>2</sub> prepared by flame synthesis, *M. J. Catal.* 272 (2010) 210–219, <https://doi.org/10.1016/j.jcat.2010.04.001>.
- [57] F. Giordanino, P.N.R. Vennestrom, L.F. Lundegaard, F.N. Stappen, S. Mossin, P. Beato, S. Bordiga, C. Lamberti, Characterization of Cu-exchanged SSZ-13: a comparative FTIR, UV-Vis, and EPR study with Cu-ZSM-5 and Cu-β with similar Si/Al and Cu/Al ratios, *Dalton Trans.* 42 (2013) 12741–12761, <https://doi.org/10.1039/c3dt50732g>.

- [58] J. Cheng, D.H. Zheng, C.N. Dai, R.N. Xu, N. Liu, G.Q. Yu, N. Wang, B.H. Chen, Constructing active copper species in Cu-zeolites for coal-gas-SCR and elucidating the synergistic catalytic function of CuO and Cu<sup>2+</sup> ion species, *Environ. Sci.: Nano.* 9 (2022) 2372, <https://doi.org/10.1039/D2EN00269H>.
- [59] J. Song, Y.L. Wang, E.D. Walter, N.M. Washton, D.H. Mei, L. Kovarik, M. H. Engelhard, S. Proding, Y. Wang, C.H.F. Peden, F. Gao, Toward rational design of Cu/SSZ-13 selective catalytic reduction catalysts: implications from atomic-level understanding of hydrothermal stability, *ACS Catal.* 7 (2017) 8214–8227, <https://doi.org/10.1021/acscatal.7b03020>.
- [60] U. Deka, I. Lezcano-Gonzalez, B.M. Weckhuysen, A.M. Beale, Local environment and nature of Cu active sites in zeolite-based catalysts for the selective catalytic reduction of NO<sub>x</sub>, *ACS Catal.* 3 (2013) 413–427, <https://doi.org/10.1021/cs300794s>.
- [61] K.A. Lomachenko, E. Borfecchia, C. Negri, G. Berlier, C. Lamberti, P. Beato, H. Falsig, S. Bordiga, The Cu-CHA deNO<sub>x</sub> catalyst in action: temperature-dependent NH<sub>3</sub>-assisted selective catalytic reduction monitored by operando XAS and XES, *J. Am. Chem. Soc.* 138 (2016) 12025–12028, <https://doi.org/10.1021/jacs.6b06809>.
- [62] J.S. McEwen, T. Anggara, W.F. Schneider, V.F. Kispersky, J.T. Miller, W.N. Delgass, F.H. Ribeiro, Integrated operando X-ray absorption and DFT characterization of Cu-SSZ-13 exchange sites during the selective catalytic reduction of NO<sub>x</sub> with NH<sub>3</sub>, *Catal. Today* 184 (2012) 129–144, <https://doi.org/10.1016/j.cattod.2011.11.037>.
- [63] S.H. Xie, W. Tan, Y.J. Li, L. Ma, S.N. Ehrlich, J.G. Deng, P. Xu, F. Gao, L. Dong, F. D. Liu, Copper single atom-triggered niobia–ceria catalyst for efficient low-temperature reduction of nitrogen oxides, *ACS Catal.* 12 (2022) 2441–2453, <https://doi.org/10.1021/acscatal.1c05661>.
- [64] H.Z. Wang, X.Z. Bi, Y.F. Yan, Y.Z. Zhao, Z.X. Yang, H. Ning, M.B. Wu, Efficient electrocatalytic reduction of CO<sub>2</sub> to ethanol enhanced by spacing effect of Cu-Cu in Cu<sub>2-x</sub>Se nanosheets, *Adv. Funct. Mater.* 33 (2023), 2214946, <https://doi.org/10.1002/adfm.202214946>.
- [65] M.K. Neylon, C.L. Marshall, A.J. Kropf, In situ EXAFS analysis of the temperature-programmed reduction of Cu-ZSM-5, *J. Am. Chem. Soc.* 124 (2002) 5457–5465, <https://doi.org/10.1021/ja0176696>.
- [66] H. Yamashita, M. Matsuoka, K. Tsuji, Y. Shioya, M. Anpo, M. Che, In-situ XAFS, photoluminescence, and IR investigations of copper ions included within various kinds of zeolites, structure of Cu(I) ions and their interaction with CO molecules, *J. Phys. Chem.* 100 (1996) 397–402, <https://doi.org/10.1021/jp952666z>.
- [67] D.D. Chen, Y.L. Yan, A.Q. Guo, V. Rizzotto, H.R. Lei, Z.W. Qiao, H. Liang, M. Jabłońska, X.Q. Jiang, J.X. Jiang, R. Palkovits, P.R. Chen, D.Q. Ye, U. Simon, Mechanistic insights into the promotion of low-temperature NH<sub>3</sub>-SCR catalysis by copper auto-reduction in Cu-zeolites, *Appl. Catal. B: Environ.* 322 (2023), 122118, <https://doi.org/10.1016/j.apcatb.2022.122118>.
- [68] C. Paolucci, A.A. Parekh, I. Khurana, J.R.D. Iorio, H. Li, J.D.A. Caballero, A.J. Shih, T. Anggara, W.N. Delgass, J.T. Miller, F.H. Ribeiro, R. Gounder, W.F. Schneider, Catalysis in a cage: condition-dependent speciation and dynamics of exchanged Cu cations in SSZ-13 Zeolites, *J. Am. Chem. Soc.* 138 (2016) 6028–6048, <https://doi.org/10.1021/jacs.6b02651>.
- [69] K. Ueda, J. Ohya, A. Satsuma, In situ XAFS study of dynamic behavior of Cu species in MFI-zeolite under element gases of ammonia selective catalytic reduction, *Chem. Lett.* 46 (2017) 1390–1392, <https://doi.org/10.1246/cl.170451>.
- [70] T.V.W. Janssens, H. Falsig, L.F. Lundegaard, P.N.R. Venneström, S.B. Rasmussen, P. G. Moses, F. Giordano, E. Borfecchia, K.A. Lomachenko, C. Lamberti, S. Bordiga, A. Godiksen, S. Mossin, P. Beato, A consistent reaction scheme for the selective catalytic reduction of nitrogen oxides with ammonia, *ACS Catal.* 5 (2015) 2832–2845, <https://doi.org/10.1021/cs501673g>.
- [71] K.A. Lomachenko, E. Borfecchia, C. Negri, G. Berlier, C. Lamberti, P. Beato, H. Falsig, S. Bordiga, The Cu-CHA deNO<sub>x</sub> catalyst in action: temperature-dependent NH<sub>3</sub>-assisted selective catalytic reduction monitored by operando XAS and XES, *J. Am. Chem. Soc.* 138 (2016) 12025–12028, <https://doi.org/10.1021/jacs.6b06809>.
- [72] P.R. Chen, A. Khetan, M. Jabłońska, J. Simböck, M. Muhler, R. Palkovits, H. Pitsch, U. Simon, Local dynamics of copper active sites in zeolite catalysts for selective catalytic reduction of NO<sub>x</sub> with NH<sub>3</sub>, *Appl. Catal. B: Environ.* 237 (2018) 263–272, <https://doi.org/10.1016/j.apcatb.2018.05.091>.
- [73] L. Chen, X.X. Wang, Q.L. Cong, H.Y. Ma, S.J. Li, W. Li, Design of a hierarchical Fe-ZSM-5@CeO<sub>2</sub> catalyst and the enhanced performances for the selective catalytic reduction of NO with NH<sub>3</sub>, *Chem. Eng. J.* 369 (2019) 957–967, <https://doi.org/10.1016/j.cej.2019.03.055>.
- [74] X.S. Liu, X.D. Wu, D. Weng, L. Shi, Modification of Cu/ZSM-5 catalyst with CeO<sub>2</sub> for selective catalytic reduction of NO<sub>x</sub> with ammonia, *J. Rare Earths* 34 (2016) 1004–1009, [https://doi.org/10.1016/S1002-0721\(16\)60127-8](https://doi.org/10.1016/S1002-0721(16)60127-8).
- [75] S. Brandenberger, O. Kröcher, A. Wokaun, A. Tisler, R. Althoff, The role of Brønsted acidity in the selective catalytic reduction of NO with ammonia over Fe-ZSM-5, *J. Catal.* 268 (2009) 297–306, <https://doi.org/10.1016/j.jcat.2009.09.028>.
- [76] B.L. Zhang, L.F. Deng, B. Liu, C.Y. Luo, M. Liebau, S.G. Zhang, R. Glaeser, Synergistic effect of cobalt and niobium in Co<sub>3</sub>-Nb-O<sub>x</sub> on performance of selective catalytic reduction of NO with NH<sub>3</sub>, *Rare Met.* 41 (2022) 166–178, <https://doi.org/10.1007/s12598-021-01790-5>.
- [77] B.L. Zhang, L.F. Deng, M. Liebau, P.Q. Wang, Y.J. Ren, B. Liu, C.Y. Luo, R. Glaeser, S.E. Zhang, Tar induced deactivation and regeneration of a commercial V<sub>2</sub>O<sub>5</sub>-MoO<sub>3</sub>/TiO<sub>2</sub> catalyst during selective catalytic reduction of NO with NH<sub>3</sub>, *Fuel* 316 (2022), 123324, <https://doi.org/10.1016/j.fuel.2022.123324>.